

Saturated reconstruction of living brain tissue

Philipp Velicky¹, Eder Miguel¹, Julia M. Michalska¹, Donglai Wei^{2,3}, Zudi Lin², Jake F. Watson¹, Jakob Troidl², Johanna Beyer², Yoav Ben-Simon^{1,4}, Christoph Sommer¹, Wiebke Jahr¹, Alban Cenameri¹, Johannes Broichhagen⁵, Seth G. N. Grant^{6,7}, Peter Jonas¹, Gaia Novarino¹, Hanspeter Pfister², Bernd Bickel¹, Johann G. Danzl^{1*}

¹Institute of Science and Technology Austria (ISTA), Klosterneuburg, Austria.

²School of Engineering and Applied Sciences, Harvard University, Cambridge, MA, USA.

³present address: Department of Computer Science, Boston College, Boston, MA, USA.

⁴present address: Dept. of Neurophysiology and Pharmacology, Vienna Medical University, Vienna, Austria.

⁵Leibniz-Forschungsinstitut für Molekulare Pharmakologie, Berlin, Germany.

⁶Genes to Cognition Program, Centre for Clinical Brain Sciences, University of Edinburgh, Edinburgh, UK.

⁷Simons Initiative for the Developing Brain (SIDB), Centre for Discovery Brain Sciences, University of Edinburgh, Edinburgh, UK.

*correspondence to: johann.danzl@ist.ac.at

Abstract

Complex wiring between neurons underlies the information-processing network enabling all brain functions, including cognition and memory. For understanding how the network is structured, processes information, and changes over time, comprehensive visualization of the architecture of living brain tissue with its cellular and molecular components would open up major opportunities. However, electron microscopy (EM) provides nanometre-scale resolution required for full *in-silico* reconstruction¹⁻⁶, yet is limited to fixed specimens and static representations. Light microscopy allows live observation, with super-resolution approaches⁷⁻¹⁵ facilitating nanoscale visualization, but comprehensive 3D-reconstruction of living brain tissue has been hindered by tissue photo-burden, photobleaching, insufficient 3D-resolution, and inadequate signal-to-noise ratio (SNR). Here we demonstrate saturated reconstruction of living brain tissue. We developed an integrated imaging and analysis technology, adapting stimulated emission depletion (STED) microscopy^{7,16} in extracellularly labelled tissue¹⁷ for high SNR and isotropic resolution. Centrally, a two-stage deep-learning approach leveraged previously obtained information on sample structure to drastically reduce photo-burden and enable automated volumetric reconstruction down to synapse level. Live reconstruction provides unbiased analysis of tissue architecture across time in relation to functional activity and targeted activation, and contextual understanding of molecular labelling. This adoptable technology will facilitate novel insights into the dynamic functional architecture of living brain tissue.

Introduction

Brain computation and information storage are intimately linked to the structure of a network of ~86 billion neurons in humans. Each is typically connected by thousands of information-transmitting synapses to other neurons and interacts with glial support cells. To address how this incredibly crowded and complex tissue's architecture, connectivity, and functional activity evolve over time and interrelate, one would ideally employ a technology that enables imaging and *in-silico* reconstruction of living brain tissue. This would allow mapping of how neuronal and non-neuronal cells and their delicate, functionally paramount subcellular specializations, such as synapses, relate to each other in the 3D tissue environment, and how this changes over time or in response to specific intervention. Combining connectivity information with the location of specific molecules could then further define cellular and subcellular identities, and provide a molecular ground truth for synapse location and type.

EM reconstruction offers the most detailed insights into brain architecture, however, it is limited to fixed specimens, static tissue representations, and sample preparation that impedes molecular labelling. A light microscopy-based technology for tissue reconstruction, in contrast, could enable observation of living systems, together with visualization of specific molecules and cellular signalling. The intricate cellular arrangements in brain tissue call for a super-resolution approach^{11,14} with resolution improvement in all three spatial dimensions, because reconstruction is limited by the lowest-resolution direction (typically along the optical axis, z -direction). Conventional (diffraction-limited) microscopy has a best-case lateral resolution of about half the wavelength of employed light and axial resolution as poor as ~ 1000 nm for tissue-compatible high-numerical aperture objective lenses and far red to infrared excitation. Here we introduce saturated reconstruction of living brain tissue. We integrate and tailor labelling, 3D-super-resolving imaging, and image processing into a pipeline that overcomes the intertwined limitations for isotropic resolving power, signal-to-noise ratio (SNR), speed, and light burden in classical super-resolution imaging. We base our technology on stimulated emission depletion (STED) microscopy^{7,16}, in which a light pattern turns off fluorophores except those located close to its intensity minimum at sub-nanosecond timescales and positions are queried sequentially. STED is thus compatible with freely diffusing fluorophores¹⁸ and is relatively robust against movement in living samples. Unlike visualization of the distribution of certain proteins or tracing the morphology of a sparse subset of cells¹⁹, saturated tissue reconstruction requires a comprehensive delineation of all cells. We therefore employed super-resolution shadow imaging¹⁷, where extracellularly applied fluorophores²⁰ define cellular structures more comprehensively than in single-molecule approaches for extracellular space imaging (ECS)²¹. Photobleached fluorophores are replenished by diffusion, and radicals generated from extracellular fluorophore bleaching are less able to damage the specimen than intracellular radicals. Despite these advantages, synapse-level reconstruction of living brain tissue has been elusive. The square-root dependence of resolution on applied STED laser power²² and the need for Nyquist sampling in 3D with low tens of nanometres step sizes impose a heavy cost of tissue photo-burden to increase 3D-resolution²³. Together with in-tissue optical imperfections that lead to progressive signal loss and lowered signal-to-noise ratio (SNR) at higher resolution, these factors ultimately limit achievable 3D-resolution and SNR²⁴. In our pipeline, we therefore specifically adapted STED for isotropically resolved tissue imaging and devised a two-stage deep learning approach to enable live-tissue compatible volumetric imaging amenable to automated saturated segmentation at synapse-level. We reduced light exposure by incorporating information on sample structure from separate, prior

measurements, using an artificial neural network to restore SNR from data collected in a high-speed, low-exposure super-resolving mode. We used a second deep neural network to translate volumetric imaging data into a saturated instance segmentation of tissue structure. We termed this technology LIONESS for *Live Information-Optimized Nanoscopy Enabling Saturated Segmentation* (**Fig. 1a**). LIONESS allows dynamic brain tissue reconstruction paired with molecular and functional information.

Results

Achieving isotropic high-SNR STED in tissue

We opted for near-infrared STED (775 nm), to deliver highest STED performance coupled with reduced tissue absorption and scattering over visible light^{23,25}. We screened for cell-impermeant fluorophores to label ECS and delineate cellular structures with maximized extra- vs. intracellular contrast, and identified suitable hydrophilic, anionic high-performance STED labels, including both unmodified commercial and custom sulfonated variants (**Suppl. Fig. 1**). We aimed for isotropic STED resolution and first incoherently overlapped classical 2π -helical and π -top-hat phase modulation patterns to achieve lateral (xy) and predominantly axial (z) STED resolution increase²⁶, respectively, and mitigated spherical aberrations on the sensitive z -STED pattern using a silicone immersion objective with correction collar. However, the resulting intensity minimum of the combined light patterns was highly susceptible to aberrations and imperfect spatial overlap in tissue. We therefore replaced the $2\pi(xy)$ -pattern with a helicity-2 mode generated by 4π -helical phase modulation²⁷. The shallower intensity rise and broader overall distribution of the $4\pi(xy)$ -STED pattern allowed more robust in-tissue alignment and improved quenching of “sidelobe” fluorescence insufficiently silenced by the z -STED pattern alone (**Suppl. Fig. 2a-c**). This led to substantially enhanced definition of cellular structures (**Suppl. Fig. 2d**). Increasing detector dynamic range improved SNR further (**Suppl. Fig. 3**). To delineate narrow spaces between cells with the extracellular label in 3D and detect the fluorescence modulation produced by thin cellular processes with sufficient SNR for segmentation, we integrated photons for $70\mu\text{s}$ per $50 \times 50 \times 50 \text{ nm}^3$ voxel and dialled in near-isotropic resolution of $\sim 130 \text{ nm}$. However, this approach was too harsh and too slow for volumetric imaging of living tissue, causing dramatic photodamage in the tissue sample (**Suppl. Fig. 4a**).

Low-exposure, high-speed STED

We thus sought for strategies to simultaneously reduce both the light burden and imaging time while augmenting SNR. To achieve this, we recorded low-exposure STED data at high speed and deployed deep-learning-based restoration to computationally increase SNR, retrieving information on sample structure from prior measurements. We trained a convolutional neural network²⁸ (**Suppl. Fig. 5a**) on paired low- and high-SNR imaging volumes of human cerebral organoids²⁹, mouse organotypic hippocampal slice cultures, and acutely prepared mouse hippocampal alveus. These contained diverse structures that were sampled at high SNR with 70 μ s voxel dwell time, from which we set aside photon counts of the first 10 μ s as low-SNR training input data. This ensured that both corresponded to voxel-exact equivalent sample structures. We could then apply this trained neural network to previously unseen data to predict high-SNR images from low-exposure input data. To evaluate the accuracy of this prediction in the context of cellular segmentation, per-voxel probabilistic uncertainty measures and ensemble disagreement between independently trained networks²⁸ were of limited utility (**Suppl. Fig. 5b**). Therefore, we compared prediction outcome with corresponding sparse, positively labelled cellular structures (**Suppl. Fig. 6a**) and with paired high-SNR measurements not included in the training (**Suppl. Fig. 6b**). This indicated that inaccuracies at the voxel level did not negatively impact delineation of cellular structures.

Repeated volumetric imaging in this low-exposure mode left cells intact, whereas they disintegrated when aiming to achieve similar resolution and SNR with the conventional high-photon load STED mode (**Suppl. Fig. 4**). Development of this scheme further reduced photon load by 86%. In contrast to current techniques²⁴ for reducing STED exposure^{30,31} and photobleaching^{32,33}, it also correspondingly sped up acquisition 7-fold and additionally denoised the data. Integrating labelling, optimizations for in-tissue isotropically resolving super-resolution imaging, low-exposure data collection, and computational SNR restoration resulted in a substantial gain in image quality over conventional STED imaging for given live-tissue compatible STED light exposure (**Fig. 1b-e**). This resulted in volumetric light-microscopy data suitable for comprehensive segmentation of living neuronal tissue.

In-silico saturated reconstruction

Manual annotation of all cellular structures in a small volume of such LIONESS imaging data showed that saturated live tissue reconstruction was feasible. However, it was time consuming and therefore poorly scalable. Segmentation of a $\sim 400 \mu\text{m}^3$ volume of living brain tissue,

selected from a highly interwoven region of neuropil in an organotypic hippocampal slice, took a trained segmenter ~450 hours (**Suppl. Fig. 7**). We therefore implemented a second deep neural network for automated segmentation, adapting algorithms and software from EM-connectomics^{34,35}, and employed an iterative training scheme. We initially trained the network on a subvolume of the manually annotated LIONESS imaging volume (285 μm^3 , the other part was used for validation) and applied it together with watershed postprocessing to larger volumes that harboured additional structural diversity. We then manually proofread the output and fed it back into training, thus extending the training volume to ~800 μm^3 for yielding an improved segmentation neural network with enhanced prediction quality.

We chose living human cerebral organoids²⁹ as first specimen for automated reconstruction, as these have emerged as powerful model systems for studying human brain development and disease mechanisms at cell to tissue level. When applied to a living cerebral organoid, our pipeline enabled saturated tissue reconstruction (**Fig. 1a**). Such samples with moderately complex tissue structure required minor intervention by manual proofreading. Reconstruction yielded contextual information not available with imaging of sparsely labelled specimens. For example, we observed the interaction of an axonal growth cone with neighbouring structures in the living organoid (**Suppl. Fig. 8**). The gain in throughput from automated over manual segmentation was substantial, with our whole pipeline including microscopic data acquisition (140 seconds), image restoration (10 seconds) and automated saturated segmentation (~40 minutes) taking less than 45 minutes excluding data inspection and proofreading (**Fig. 1e**). Manual segmentation would require an estimated ~860 person-hours for this organoid dataset (1,737 μm^3). Extracting the space not occupied by cellular segments additionally allowed us to reconstruct the ECS, which amounted to 225 μm^3 or 13% in this organoid subvolume (**Suppl. Fig. 9**).

In the next step, we chose the alveus of intact, acutely dissected mouse hippocampi, a region that is extremely densely packed with thin neuronal processes transmitting signals to other regions. Automated reconstruction highlighted the thin, individually resolved axons running in various orientations and interacting with glial cells (**Suppl. Fig. 10a,b,c, Suppl. Video 1, 2**). Such dense but structurally comparatively homogeneous regions also required little intervention during proofreading. Approximately 45 corrections per mm axon length were necessary in such data, with false splits being the dominant type of error (**Suppl. Fig. 10d**). These data showed that a comprehensive structural segmentation of living nervous tissue is feasible.

Validation of segmentation

To test the potential of this technology for saturated reconstruction and analysis of complex nervous tissue specimens, we collected imaging volumes from the highly interwoven neuropil in organotypic hippocampal slices. These volumes contained diverse neuronal structures from spiny dendrites, to axons and their boutons, and astrocytic processes. We focused on assignment of dendritic spines to dendrite branches, as the fine connecting spine necks are among the thinnest of neuronal structures^{36,37}. We tested our reconstruction capability against sparse structural ground truth from cytosolic EGFP expression, which revealed all dendritic spines on a given dendrite. From LIONESS imaging data alone, without automated segmentation, a neuroscientist blinded to EGFP ground truth data detected 73% ($\pm 8.3\%$, mean \pm standard deviation, s.d.) of spines in four different example dendrite stretches (from three independent biological replicates). When applied to the same datasets, the artificial network often segmented and correctly connected spines to the respective dendrite or classified spines as separate (orphan) segments which could then be unambiguously assigned to a dendrite. The experimenter who collected the data performed proofreading of the segmentation output and correctly attached 83% ($\pm 8.0\%$, mean \pm s.d.) of dendritic spines (**Fig. 2, Suppl. Fig. 11**). This showed that both manual and automated reconstruction can retrieve a large percentage of dendritic spines and demonstrated applicability of LIONESS for analysis of neuropil architecture.

Connectivity reconstruction

We now applied our technology to living hippocampal CA1 neuropil to unbiasedly visualize the architecture of this complex region. We identified and reconstructed diverse cellular constituents like myelinated and unmyelinated axons, spiny dendrites, and glial cells in the densely packed tissue volume (**Fig. 3 a, b, Suppl. Fig. 12a, Suppl. Video 3, 4**). Similar as with EM, proofreading of automated segmentation remains a time-limiting factor, such that it is often preferable to selectively apply it to the specific structures of interest. We focused reconstruction on an individual dendrite, revealing 38 spines that showed various morphologies, including thin, branched, mushroom-shaped, and filopodial (**Fig. 3c**). Spine heads were of diverse 3D-shapes, some hand-like engulfing part of the presynaptic bouton. Spine lengths ranged from 0.54 μm to 3.96 μm ($1.77 \mu\text{m} \pm 0.69 \mu\text{m}$, mean \pm s.d.) and showed a unimodal distribution (**Fig. 3d**). We identified 28 axons where a bouton directly contacted a spine head, resulting in a total of 39 putative synapses along these 22 μm of reconstructed

dendrite (**Fig. 3c, Suppl. Fig. 12b**). Most axons made single (20) or double (6) connections, however triple and quadruple spine contacting axons were also observed. We did not observe a preferred angular orientation of contacting axons with respect to the dendritic shaft, further demonstrating the complex arrangement of the CA1 neuropil. The mean density of spines was $1.7/\mu\text{m}$ dendrite length. Both, length and density quantifications are in-keeping with previous data³⁸. **Fig. 3e** details spine length and position along the dendrite for each spine, together with exemplary volumetric renderings of pre- and postsynaptic structures.

Molecularly informed reconstruction

We next sought to integrate key methods for live molecular labelling into tissue reconstruction. Live affinity labels proved useful for corroborating identity of specific structures, like myelinated axons (**Suppl. Fig. 13**). Most importantly, light microscopy is unrivalled at visualizing specific protein locations. As mere proximity of spine and bouton can be a poor predictor of synaptic connectivity between neurons¹, we complemented it with a molecular definition of synaptic sites. We used a mouse line expressing a HaloTag³⁹ fused to endogenous PSD95 protein^{40,41}, an abundant protein located in the postsynaptic terminal of excitatory synapses. Irreversible binding of applied Halo ligands coupled to a fluorescent dye visualized all postsynaptic excitatory terminals. In addition, we applied a combination of adeno-associated virus (AAV) and pseudotyped rabies particles⁴² to induce expression of EGFP-coupled synaptophysin, visualizing pre-synaptic terminals (**Fig. 4a, Suppl. Fig. 14, Suppl. Video 5**). These pre- and postsynaptic markers were combined with 3D-structural LIONESS imaging in the CA1 neuropil, providing cellular context lacking with conventional molecular labelling. Combined structural and molecular information unambiguously revealed various types of connections between pre- and postsynaptic partners: boutons of two separate axons converging on a single spine, single boutons contacting two neighbouring spines of the same dendrite, and textbook-like single bouton to single spine connections (**Fig. 4b**). Excitatory synapses are preferentially located at dendritic spines, however also occur on dendritic shafts, in particular on aspiny interneurons. We also used the combined molecular and structural information to determine the fraction of excitatory synapses with dendritic shaft location in our imaging volumes, equalling 8.3% in **Fig. 4** and 14.7% in **Suppl. Fig. 14**. Of note, comparison with diffraction-limited readout of synaptic molecules further illustrated the gain in 3D-definition with LIONESS (**Fig. 4a, bottom, Suppl. Fig. 14b, bottom**).

Morphodynamics and activity

Our low-exposure approach allowed repeated reconstruction of the same tissue volume, revealing how subcellular morphologies and the neuronal network evolved over time, and direct pairing with optical readout of activity. We first used LIONESS to repeatedly image the same volume of hippocampal neuropil over 3 days. This allowed us to observe morphology changes and movement of neuronal and non-neuronal subcellular structures in their context (**Suppl. Fig. 15**), rather than being limited to sparse, positively labelled cells¹⁹.

We now devised an all-optical approach to correlate 3D-structure and signalling activity in the same cellular network. We focused on the hippocampal circuitry, where mossy fibres originating from dentate gyrus (DG) granule cells deliver excitatory input to the proximal dendrites of pyramidal neurons in the CA3 region, forming boutons on complex spines often termed thorny excrescences⁴³ (**Suppl. Fig. 16a, b**). Using organotypic slices from a mouse line where all DG granule cells expressed the calcium indicator GCaMP6s⁴⁴ (Ai95/Prox1-cre) we recorded calcium transients in individual mossy fibre boutons with sub-second resolution, applying pharmacological manipulation with the GABA_A receptor antagonist gabazine to enhance network activity. LIONESS revealed the underlying 3D-cellular organization (**Suppl. Fig. 16c, d, Suppl. Video 6, 7**). Furthermore, both mossy fibre boutons and their postsynaptic complex spines showed structural dynamics on the minutes timescale. Signalling activity continued during LIONESS acquisition (**Suppl. Fig. 16b,e**).

We next developed a more refined approach for investigating activity and dynamics within the tissue, combining chemogenetically targeted cell activation with Ca²⁺-imaging and dynamic reconstruction. We expressed the virally encoded DREADD (designer receptor exclusively activated by designer drugs)⁴⁵ hM3Dq in a subset of DG granule cells, which enhanced neuronal excitation upon application of the bio-orthogonal drug clozapine N-oxide (CNO). This allowed us to control and image the activity of a mossy fibre bouton (**Fig. 5a, Suppl. Video 8**), before structurally reconstructing it together with the postsynaptic complex spine on a CA3 pyramidal neuron. We visualized the structural evolution after 19.5h (**Fig. 5b**), which revealed dramatic rearrangements in synaptic architecture, mirrored in a bouton volume change from 11.8 μm^3 to 8.3 μm^3 . With its applicability to living tissue, LIONESS has the capability to determine structure-function relationships in neuronal tissue.

Electrophysiology

We reasoned that with LIONESS, light microscopy may not only be used for visual guidance of electrophysiology experiments, but to correlate electrical properties of single and synaptically connected pairs of neurons with the underlying neuronal architecture. We performed whole-cell patch-clamp recordings of two neighbouring pyramidal neurons in the hippocampal CA1 region, taking advantage of the fact that these cells often form monosynaptic connections in organotypic culture⁴⁶. Cells with confirmed synaptic connectivity were imaged post-recording (**Suppl. Fig. 17**), first in diffraction-limited mode with fluorophores intracellularly applied during recording, and then with LIONESS. Zooming in on a region of putative contact, diffraction-limited readout indicated that this was the site of electrophysiologically confirmed communication. Only comprehensive 3D-super-resolved delineation in the LIONESS volume revealed the deception by disclosing an intervening, unlabelled neuronal process missed in diffraction-limited mode. This corroborated that LIONESS was suitable for a multimodal approach to correlate structural with functional aspects of tissue architecture, and more powerful in doing so than diffraction-limited imaging.

Bridging scales

Analysis of tissue architecture was not limited to single LIONESS volumes. For extending analysis volumes and embedding them into meso-scale context, we followed two straightforward approaches. Firstly, recording multiple partially overlapping subvolumes in the living tissue allowed automatically 3D-registering them with sufficient accuracy, such that segments from automated reconstruction smoothly extended over the borders. For example, we reconstructed a 70 μm -long stretch of mostly parallel axon fibres in acutely prepared mouse alveus from four image volumes – thus capturing ~ 3 mm of cumulative axon length in this continuous region (**Suppl. Fig. 18**). Secondly, we guided selection of LIONESS volumes by recording larger volumes with diffraction-limited resolution, which provided further context to reconstructed regions. As one example, imaging a 650,000 μm^3 volume in the DG crest of the hippocampus gave positional context and allowed identification of larger objects like cell somata and major dendritic branches, whereas LIONESS reconstruction revealed how DG granule cell and other cellular processes were embedded in the invaginations of a glial cell (**Suppl. Fig. 19, Suppl. Video 9, 10**). Imaging across spatial scales thus yields information on cell position and identity to extend the interpretation of connectivity analysis made possible by LIONESS.

Discussion

Here, we demonstrate saturated reconstruction of living mammalian brain tissue. This allowed tracking the time evolution of its structure and direct pairing with information on molecule location and activity. Together, these elements constitute a fundamentally new quality of information for the study of brain structure and function, overcoming limitations of both static EM representations and reconstruction of positively labelled, incomplete subsets of tissue constituents in light microscopy.

To achieve this, we developed a technology integrating optimization of optical tissue imaging with a two-step deep-learning strategy for imaging and segmenting living brain tissue. It may come as a surprise that a moderate ~ 130 nm isotropic 3D-resolution, chosen to limit burden on the living specimen, was sufficient for brain tissue reconstruction. This contrasts with ~ 4 x better resolution in the worst-resolved direction in typical EM reconstructions^{1,2}, relying on physical sectioning into ~ 30 nm thick slices. Four factors aided segmentation: 1) Extracellular labelling selectively highlighted the space separating cellular structures. The presence of a separating fluorophore layer was detectable also at resolution worse than the thickness of this layer. ECS labelling eclipsed complexity from intracellular organelles in the cell segmentation channel, whereas specific labelling revealed intracellular structures and molecules in spectrally distinct detection channels. 2) Also cellular structures smaller than the effective point-spread-function of the microscope led to modulation of fluorescence counts by volume exclusion of extracellular label, aiding in their detection. 3) Live imaging lacks alterations of tissue structure from chemical fixation, including shrinkage⁴⁷ of the space filled with label in between cells. 4) Optical sectioning yields inherently aligned volumetric stacks, avoiding potential technical challenges with alignment after physical sectioning.

Our parameter search for image acquisition, processing, and segmentation was in no way exhaustive, opening possibilities for future improvements. For example, beyond brute-force further extension of the training bases for both deep-learning networks, the first network may be trained on paired low/high-exposure volumes where the high-exposure ground truth also features increased resolution. LIONESS will likely benefit from specifically engineered fluorophores for high performance extracellular labelling, which we have only started to explore by attaching hydrophilicity-enhancing sulfonate groups.

Our chosen LIONESS volumes of up to $\sim 4,500 \mu\text{m}^3$ reflect best optical performance within a few tens of μm depth and in the central region of the objective's field of view. We increased these laterally via volumetric tiling whereas adaptive optics⁴⁸ may be used to enhance axial

range. Rather than maximizing imaging volumes, one may also bridge scales with complementary methods, such as viral tracing. While we used rabies virus for live labelling of synapses, this approach may be extended to retrogradely trace^{42,49} the cellular origins of synaptic input identified in LIONESS. Application of LIONESS in living animals harbours engineering challenges due to movement⁵⁰ that may be addressed by developing motion-compensating algorithms. We envision that correlating live information from LIONESS with light microscopy measurements of the same specimen after fixation will be useful, as this opens up further possibilities for molecular characterization and large-scale super-resolution tissue imaging⁵¹. Such all-optical correlative measurements will be considerably less complex than correlative approaches with EM. As expected, optimum sample and imaging conditions were required for full reconstruction. However, STED imaging was performed on a commercial microscope with minor adaptations, which underscores adoptability of this technology. The simplified workflow and lower demands in equipment or personnel of LIONESS compared to serial-sectioning or block-face imaging EM should enable analysis of multiple specimens as a function of genotype, developmental stage, disease, or specific intervention.

LIONESS has the capability to analyse the structure of living brain tissue in a comprehensive, unbiased way, providing rich opportunities for unexpected discoveries. Unlike with sparse cellular labelling, LIONESS resolves structures with their interacting partners. This provides resolution of both neuronal input and output, and facilitates observation of synaptic heterogeneity, which underlies much of the complexity of the brain. We extracted exemplary quantitative data on neuronal connectivity and structure to showcase that LIONESS provides quantitative, dynamical biological information. We thus expect it to facilitate addressing biological questions related to stability and rewiring of network structure⁵², the dynamics of neuron-glia interactions and ECS, and structure-function relationships. LIONESS opens up new avenues for decoding complex tissue architecture in living mammalian brain and other organs.

References

1. Kasthuri, N. *et al.* Saturated Reconstruction of a Volume of Neocortex. *Cell* **162**, 648–661 (2015).

2. Motta, A. *et al.* Dense connectomic reconstruction in layer 4 of the somatosensory cortex. *Science* **366**, (2019).
3. Turner, N. L. *et al.* Reconstruction of neocortex: Organelles, compartments, cells, circuits, and activity. *Cell* (2022) doi:10.1016/j.cell.2022.01.023.
4. Briggman, K. L., Helmstaedter, M. & Denk, W. Wiring specificity in the direction-selectivity circuit of the retina. *Nature* **471**, 183–188 (2011).
5. Shapson-Coe, A. *et al.* A connectomic study of a petascale fragment of human cerebral cortex. *bioRxiv* 2021.05.29.446289 (2021) doi:10.1101/2021.05.29.446289.
6. Januszewski, M. *et al.* High-precision automated reconstruction of neurons with flood-filling networks. *Nature Methods* **15**, 605–610 (2018).
7. Klar, T. A., Jakobs, S., Dyba, M., Egner, A. & Hell, S. W. Fluorescence microscopy with diffraction resolution barrier broken by stimulated emission. *Proceedings of the National Academy of Sciences* **97**, 8206–8210 (2000).
8. Rust, M. J., Bates, M. & Zhuang, X. Sub-diffraction-limit imaging by stochastic optical reconstruction microscopy (STORM). *Nature Methods* **3**, 793–796 (2006).
9. Betzig, E. *et al.* Imaging Intracellular Fluorescent Proteins at Nanometer Resolution. *Science* **313**, 1642–1645 (2006).
10. Hess, S. T., Girirajan, T. P. K. & Mason, M. D. Ultra-high resolution imaging by fluorescence photoactivation localization microscopy. *Biophysical Journal* **91**, 4258–4272 (2006).
11. Sahl, S. J., Hell, S. W. & Jakobs, S. Fluorescence nanoscopy in cell biology. *Nature Reviews Molecular Cell Biology* **18**, 685–701 (2017).
12. Giannone, G. *et al.* Dynamic Superresolution Imaging of Endogenous Proteins on Living Cells at Ultra-High Density. *Biophysical Journal* **99**, 1303–1310 (2010).

13. Heilemann, M. *et al.* Subdiffraction-resolution fluorescence imaging with conventional fluorescent probes. *Angewandte Chemie - International Edition* **47**, 6172–6176 (2008).
14. Sigal, Y. M., Zhou, R. & Zhuang, X. Visualizing and discovering cellular structures with super-resolution microscopy. *Science* **361**, 880–887 (2018).
15. Chen, F., Tillberg, P. W. & Boyden, E. S. Expansion microscopy. *Science* **347**, 543–548 (2015).
16. Hell, S. W. & Wichmann, J. Breaking the diffraction resolution limit by stimulated emission: stimulated-emission-depletion fluorescence microscopy. *Optics Letters* **19**, 780 (1994).
17. Tønnesen, J., Inavalli, V. V. G. K. & Nägerl, U. V. Super-Resolution Imaging of the Extracellular Space in Living Brain Tissue. *Cell* **172**, 1108-1121.e15 (2018).
18. Kastrup, L., Blom, H., Eggeling, C. & Hell, S. W. Fluorescence Fluctuation Spectroscopy in Subdiffraction Focal Volumes. *Physical Review Letters* **94**, 178104 (2005).
19. Nägerl, U. V., Willig, K. I., Hein, B., Hell, S. W. & Bonhoeffer, T. Live-cell imaging of dendritic spines by STED microscopy. *Proceedings of the National Academy of Sciences* **105**, 18982–18987 (2008).
20. Kitamura, K., Judkewitz, B., Kano, M., Denk, W. & Häusser, M. Targeted patch-clamp recordings and single-cell electroporation of unlabeled neurons in vivo. *Nature Methods* **5**, 61–67 (2008).
21. Godin, A. G. *et al.* Single-nanotube tracking reveals the nanoscale organization of the extracellular space in the live brain. *Nature Nanotech* **12**, 238–243 (2017).
22. Harke, B. *et al.* Resolution scaling in STED microscopy. *Optics Express* **16**, 4154 (2008).
23. Kilian, N. *et al.* Assessing photodamage in live-cell STED microscopy. *Nat Methods* **15**, 755–756 (2018).

24. Jahr, W., Velicky, P. & Danzl, J. G. Strategies to maximize performance in STimulated Emission Depletion (STED) nanoscopy of biological specimens. *Methods* **174**, 27–41 (2020).
25. Göttfert, F. *et al.* Coaligned Dual-Channel STED Nanoscopy and Molecular Diffusion Analysis at 20 nm Resolution. *Biophysical Journal* **105**, L01–L03 (2013).
26. Keller, J., Schönle, A. & Hell, S. W. Efficient fluorescence inhibition patterns for RESOLFT microscopy. *Optics Express* **15**, 3361 (2007).
27. Saleh, B. E. A. & Teich, M. C. *Fundamentals of Photonics*. (John Wiley & Sons, 2007). doi:10.1002/0471213748.
28. Weigert, M. *et al.* Content-aware image restoration: pushing the limits of fluorescence microscopy. *Nat Methods* **15**, 1090–1097 (2018).
29. Lancaster, M. A. *et al.* Cerebral organoids model human brain development and microcephaly. *Nature* **501**, 373–379 (2013).
30. Staudt, T. *et al.* Far-field optical nanoscopy with reduced number of state transition cycles. *Optics Express* **19**, 5644 (2011).
31. Heine, J. *et al.* Adaptive-illumination STED nanoscopy. *Proceedings of the National Academy of Sciences* **114**, 9797–9802 (2017).
32. Danzl, J. G. *et al.* Coordinate-targeted fluorescence nanoscopy with multiple off states. *Nature Photonics* **10**, 122–128 (2016).
33. Donnert, G. *et al.* Macromolecular-scale resolution in biological fluorescence microscopy. *Proceedings of the National Academy of Sciences* **103**, 11440–11445 (2006).
34. Lin, Z., Wei, D., Lichtman, J. & Pfister, H. PyTorch Connectomics: A Scalable and Flexible Segmentation Framework for EM Connectomics. *arXiv preprint arXiv:2112.05754* (2021).

35. Lee, K., Zung, J., Li, P., Jain, V. & Seung, H. S. Superhuman Accuracy on the SNEMI3D Connectomics Challenge. *arXiv preprint arXiv:1706.00120* (2017).
36. Tønnesen, J., Katona, G., Rózsa, B. & Nägerl, U. V. Spine neck plasticity regulates compartmentalization of synapses. *Nat Neurosci* **17**, 678–685 (2014).
37. Ofer, N., Berger, D. R., Kasthuri, N., Lichtman, J. W. & Yuste, R. Ultrastructural analysis of dendritic spine necks reveals a continuum of spine morphologies. *Develop. Neurobiol.* **81**, 746–757 (2021).
38. Barón-Mendoza, I. *et al.* Changes in the Number and Morphology of Dendritic Spines in the Hippocampus and Prefrontal Cortex of the C58/J Mouse Model of Autism. *Front. Cell. Neurosci.* **15**, 726501 (2021).
39. Encell, L. P. *et al.* Development of a dehalogenase-based protein fusion tag capable of rapid, selective and covalent attachment to customizable ligands. *Curr Chem Genomics* **6**, 55–71 (2012).
40. Bulovaite, E. *et al.* A brain atlas of synapse protein lifetime across the mouse lifespan. *bioRxiv* 2021.12.16.472938 (2021) doi:10.1101/2021.12.16.472938.
41. Masch, J.-M. *et al.* Robust nanoscopy of a synaptic protein in living mice by organic-fluorophore labeling. *Proceedings of the National Academy of Sciences* **115**, E8047–E8056 (2018).
42. Sumser, A., Joesch, M., Jonas, P. & Ben-Simon, Y. An extended toolkit for production and use of RVdG-CVS-N2c rabies viral vectors uncovers hidden hippocampal connections. *bioRxiv* 2021.12.23.474014 (2021) doi:10.1101/2021.12.23.474014.
43. Rollenhagen, A. *et al.* Structural Determinants of Transmission at Large Hippocampal Mossy Fiber Synapses. *Journal of Neuroscience* **27**, 10434–10444 (2007).
44. Chen, T.-W. *et al.* Ultrasensitive fluorescent proteins for imaging neuronal activity. *Nature* **499**, 295–300 (2013).

45. Alexander, G. M. *et al.* Remote Control of Neuronal Activity in Transgenic Mice Expressing Evolved G Protein-Coupled Receptors. *Neuron* **63**, 27–39 (2009).
46. Debanne, D., Guerineau, N. C., Gahwiler, B. H. & Thompson, S. M. Physiology and pharmacology of unitary synaptic connections between pairs of cells in areas CA3 and CA1 of rat hippocampal slice cultures. *Journal of Neurophysiology* **73**, 1282–1294 (1995).
47. Korogod, N., Petersen, C. C. & Knott, G. W. Ultrastructural analysis of adult mouse neocortex comparing aldehyde perfusion with cryo fixation. *eLife* **4**, e05793 (2015).
48. Velasco, M. G. M. *et al.* 3D super-resolution deep-tissue imaging in living mice. *Optica* **8**, 442–450 (2021).
49. Wickersham, I. R., Finke, S., Conzelmann, K.-K. & Callaway, E. M. Retrograde neuronal tracing with a deletion-mutant rabies virus. *Nat Methods* **4**, 47–49 (2007).
50. Berning, S., Willig, K. I., Steffens, H., Dibaj, P. & Hell, S. W. Nanoscopy in a Living Mouse Brain. *Science* **335**, 551–551 (2012).
51. Gao, R. *et al.* Cortical column and whole-brain imaging with molecular contrast and nanoscale resolution. *Science* **363**, eaau8302 (2019).
52. Attardo, A., Fitzgerald, J. E. & Schnitzer, M. J. Impermanence of dendritic spines in live adult CA1 hippocampus. *Nature* **523**, 592–596 (2015).
53. Schindelin, J. *et al.* Fiji: an open-source platform for biological-image analysis. *Nat Methods* **9**, 676–682 (2012).
54. Ben-Simon, Y. *et al.* Entorhinal layer 6b subplate neurons govern spatial learning and memory. *bioRxiv* 2022.01.26.477814 (2022) doi:10.1101/2022.01.26.477814.
55. Armbruster, B. N., Li, X., Pausch, M. H., Herlitze, S. & Roth, B. L. Evolving the lock to fit the key to create a family of G protein-coupled receptors potently activated by an inert ligand. *Proceedings of the National Academy of Sciences* **104**, 5163–5168 (2007).

56. Guzman, S. J., Schlögl, A. & Schmidt-Hieber, C. Stimfit: quantifying electrophysiological data with Python. *Front Neuroinform* **8**, 16 (2014).
57. Krull, A., Buchholz, T.-O. & Jug, F. Noise2Void - Learning Denoising from Single Noisy Images. *arXiv:1811.10980 [cs]* (2019).
58. Berger, D. R., Seung, H. S. & Lichtman, J. W. VAST (Volume Annotation and Segmentation Tool): Efficient Manual and Semi-Automatic Labeling of Large 3D Image Stacks. *Frontiers in Neural Circuits* **12**, (2018).
59. Zlateski, A. & Seung, H. S. Image Segmentation by Size-Dependent Single Linkage Clustering of a Watershed Basin Graph. *CoRR* **abs/1505.00249**, (2015).
60. Jorstad, A., Blanc, J. & Knott, G. NeuroMorph: A Software Toolset for 3D Analysis of Neurite Morphology and Connectivity. *Frontiers in Neuroanatomy* **12**, (2018).
61. Jakob Troidl, M. H., Corrado Cali, Eduard Gröller, Hanspeter Pfister & Beyer, J. Barrio: Customizable Spatial Neighborhood Analysis and Comparison for Nanoscale Brain Structures. *submitted* (2022).

Author contributions

P.V. designed and performed experiments, analysed, proofread, and visualized data, and prepared figures. E.M. set up and performed automated segmentation, data analysis, and visualization. J.M.M. supported experiments. D.W. and Z.L. supported automated segmentation. J.W. performed patch-clamp experiments and segmentation for validation. J.T. performed visualization, advised by J.Be.. Y.B.-S. provided viral constructs. C.S. supported image analysis. W.J. supported setting up imaging and troubleshooting. A.C. performed manual segmentations. J.Br. synthesized SulfoAtto 643. S.G.N.G. provided PSD95-HaloTag mouse. P.J. supervised patch clamp experiments and virus generation. G.N. advised on and provided human cerebral organoids. H.P. advised on automated segmentation. B.B. supervised computer vision. J.G.D. conceived and supervised the study, designed experiments, and interpreted data. J.G.D. wrote the paper together with P.V. with critical input from all authors.

Competing interests

The authors declare no competing interests.

Acknowledgements

We thank J. Vorläufer, N. Agudelo, A. Wartak for microscope maintenance and troubleshooting, C. Kreuzinger and A. Freeman for technical assistance, and J. Lyudchik and M. Šuplata for computational support and hardware control and Márcia Cunha dos Santos for initial exploration of software. We thank Paul Henderson for advice on deep-learning training and Michael Sixt, Scott Boyd, and Tamara Weiss for discussions and critical reading of the manuscript. Luke Lavis (Janelia Research Campus) generously provided JF585-HaloTag ligand. We acknowledge expert support by IST Austria's scientific computing, bioimaging, preclinical, and life science facilities, and by the Miba machine shop.

This work was supported by the Austrian Science Fund (FWF) to J.G.D. (I3600-B27 and DK W1232), by the Gesellschaft für Forschungsförderung NÖ (NFB) to J.G.D. (LSC18-022), an institutional (ISTA) Interdisciplinary Project grant to J.G.D. and B.B., a postdoctoral fellowship from the Human Frontier Science Program (HFSP) to W.J. (LT000557/2018), the European Research Council (ERC) under the European Union's Horizon 2020 research and innovation programme to B.B. (715767 – MATERIALIZABLE), to G.N. (715508 – REVERSEAUTISM), and to S.G. (695568 – SYNNOVATE), the Simons Foundation Autism Research Initiative to S.G. (529085), and the Wellcome Trust to S.G. (Technology Development Grant 202932). This work was also partially supported by NSF grants IIS-1835231 and NCS-FO-2124179 to H.P..

Methods

Animals

Animals were housed in groups of 3–4 animals per cage and kept on a 12 h light/dark cycle (lights on at 7:00 am), with food and water available ad libitum. If not stated otherwise, we used wild-type C57BL/6J mice. All transgenic lines (see Table 1) used in this study have been previously characterized. For experimental use, we crossed Ai95 and Prox1-cre. For experiments with PSD95-HaloTag mice^{40,41}, both homozygous and heterozygous animals were used. For all experiments, male and female mice were used interchangeably. Experiments and

procedures were performed in strict accordance with institutional, national, and European guidelines for animal experimentation.

Transgenic line	Full name	Source (deposited by)	Cat#
Ai95	B6;129S-Gt(ROSA)26Sortm95.1(CAG-GCaMP6f)Hze/J	Jackson labs (H. Zeng)	024105
Prox1-cre	Tg(Prox1-cre)SJ32Gsat/Mmucd	MMRRC (N. Heintz)	036644-UCD
PSD95-HaloTag	PSD95-HaloTag	Seth G. N. Grant, Edinburgh	-
Thy1-EGFP	STOCK Tg(Thy1-EGFP)MJrs/J	Jackson labs (J. Sanes)	007788

Table 1

Organotypic Hippocampal slice cultures

Hippocampal slices were obtained from 5-7 days old mice of either sex and cultured on cell culture inserts with porous membranes. Mouse pups were decapitated and the hippocampus was isolated while the brain was submerged in ice cold sterile filtered HBSS without Ca^{2+} and Mg^{2+} (Gibco, #14175-053) supplemented with 10 mM glucose, using a stereo microscope. Hippocampi were cut into 350 μm thick slices and placed on round porous membranes with 4 mm diameter (PTFE membrane, Merck, #FHLC01300), which have been placed on cell culture inserts with a porous membrane (Millicell, #PICM0RG50) for interface culture. The inserts with the slices were placed in dishes (Greiner, 627161) with 1 ml of culture media. We adapted the media recipe during the course of experiments, as quality of cultures deteriorated with the same nominal composition. We found 78.5% Minimum Essential Medium (MEM), 15% heat-inactivated horse serum, 2% B27 supplement, 2.5% 1 M HEPES, 1.5% 0.2 M GlutaMax supplement, 0.5% 0.05 M ascorbic acid, with additional 1 mM CaCl_2 and 1 mM MgSO_4 to produce satisfactory results, and incubated at 37 °C and 5% CO_2 . The medium was changed the day after preparation and then every 3-4 days.

ECS labelling

For ECS labelling, artificial cerebrospinal fluid (ACSF) was prepared from a 10x stock solution with MgCl_2 and CaCl_2 added freshly before carbogen bubbling, whereas ascorbic acid and Trolox were added after bubbling. Finally, ACSF consisted of 125 mM NaCl, 2 mM CaCl_2 , 1.3 mM MgCl_2 , 4.8 mM KCl, 26 mM NaHCO_3 , 1.25 mM NaH_2PO_4 , 7.5 mM HEPES, 20 mM D-glucose, 1 mM Trolox, 1 mM ascorbic acid; pH 7.4. Thereafter, fluorescent dye (Atto 643 (Atto-Tec GmbH, #AD 643-25), SulfoAtto 643, or Abberior STAR 635P (Abberior,

#ST635P)) was added from 5 mM stocks (dissolved in ACSF) to a final concentration of 150 μ M. A 2 μ l droplet of the dye-containing imaging solution was put on a #1.5H coverslip that had been placed in an imaging chamber (RC-41, Warner Instruments). Using fine forceps, brain slices with the membrane attached were then carefully put onto the droplet, such that the slice was oriented towards the coverslip. A slice anchor gently kept the sample in place. Immediately afterwards, further imaging solution at room temperature (RT) was added. The imaging chamber was then placed onto the stage adapter of the STED microscope (see below). The data in the manuscript were acquired using Atto 643, except for **Fig. 5** and **Suppl. Fig. 11** (left panel) where SulfoAtto 643 was used.

Acutely prepared hippocampus imaging

Hippocampi were extracted from 5-7 days old mice of either sex. Mouse pups were decapitated and the hippocampus isolated while the brain was submerged in ice cold sterile filtered HBSS without Ca^{2+} and Mg^{2+} (Gibco, #14175-053) supplemented with 10 mM glucose, using a stereo microscope. The whole hippocampus was then submerged in freshly carbogenized ACSF with 150 μ M Atto 643 dye and incubated for 10 min at RT with gentle agitation. Afterwards, hippocampi were placed on a #1.5H coverslip that had been placed in an imaging chamber (RC-41, Warner Instruments). A slice anchor gently kept the sample in place when freshly carbogenized ACSF with 150 μ M Atto 643 dye was added for imaging. The imaging chamber was then placed onto the stage adapter of the STED microscope.

Generation of cerebral organoids

Human embryonic stem cells were dissociated to single cells using Accutase. A total of 2500 cells was transferred to each well of an ultra-low-binding-96-well plate (Corning) in mTeSR1 media supplemented with 50 μ M Y-27632. Cells were allowed to aggregate to EBs and fed every second day. At day 3 supplements were removed and from day 6 the generation of cerebral organoids was performed according to Lancaster and Knoblich²⁰. Briefly, EBs were transferred to neural induction medium (NIM) in low-adhesion 24-well plates (Corning), and fed every second day for 5 days until formation of neuroepithelial tissue (day 0 of cerebral organoid formation). Neuroepithelial tissue-displaying organoids were embedded in Matrigel droplets (Corning, #356234) and grown in cerebral organoid medium (COM) supplemented with B27 without vitamin A (Gibco) and fed every other day. After 4 days tissues were transferred to COM supplemented with B27 containing vitamin A and placed on a horizontal shaker at 70-100rpm. Cerebral organoids were fed twice a week.

LIONESS imaging

STED microscopy was performed at room temperature on an inverted Expert Line STED microscope (Abberior Instruments) with pulsed excitation and STED lasers. A 640 nm laser was used for excitation and a 775 nm laser for stimulated emission. A silicone oil immersion objective with 1.35 NA and a correction collar (Olympus, UPLSAPS 100XS) was used for image acquisition. The fluorescence signal was collected in a confocal arrangement with a pinhole size of 0.6 or 0.8 airy units. For detection a 685/70 nm bandpass filter was used and a 50:50 beam splitter (Thorlabs, #BSW29R) distributed the signal onto two photon counting avalanche photodiodes, allowing for stronger excitation without saturating detectors. Both detection channels were added up using Fiji⁵³ Version: 2.3.0/1.53f (Fiji/process/calculator plus/add), photon counts inverted, and data saved in 16-bit TIFF format. The pulse repetition rate was 40 MHz and fluorescence detection was time-gated. LIONESS volumes were acquired with 10 μ s pixel dwell time, 2.9 μ W (640 nm) excitation laser power and 90 mW STED laser power. A spatial light modulator (SLM) imprinted incoherently overlapped phase patterns for predominantly axial resolution increase (π -tophat phase modulation, z-STED), and for predominantly improved fluorescence quenching outside the central minimum (4π -helical phase modulation, $4\pi(xy)$ -STED) onto the STED beam. The SLM was also used to perform alignment directly in the sample, ensuring that the intensity minima of the two STED patterns spatially coincided and to optionally adjust low-order Zernicke polynomials for empirical aberration correction. Power ratio of z-STED/ $xy(4\pi)$ -STED/ was 80/20. Voxel size was 50 x 50 x 50 nm³ for all images. Acquisition scan mode was typically xzy , with the y -direction being the slowest scan axis, using galvanometric mirrors for lateral (xy)-scanning and a sample piezo stage (Physik Instrumente (PI) GmbH & Co. KG, #P-736.ZRO) for axial (z)-scanning.

For samples with additional positive labels (HaloTag ligand JF585, Synaptophysin-EGFP, Thy-1-EGFP, GCaMP6s), additional colour channels with diffraction-limited resolution using a 488 nm or 560 nm laser with 10 μ s dwell time and 1.1 – 3.9 μ W (488 nm) and 2 – 2.6 μ W (560 nm) excitation power were used for recordings. These signals were collected using a photon counting avalanche photodiode with a 525/50 nm and 605/50 nm bandpass filters for EGFP and JF585 detection, respectively. The 488 nm and 640 nm excitations were done simultaneously, for 560 nm excitation a second line step was used to avoid spectral bleed-through into the far-red channel. Voxel size was again 50 x 50 x 50 nm³ for all images with

xzy-scan mode. The power values refer to the power at the sample, measured with a slide powermeter head (Thorlabs, S170C).

Repeated volumetric live imaging

For evaluation of tissue photo-burden with LIONESS vs. conventional high-exposure STED (**Suppl. Fig. 4**) a 70 x 70 μm confocal overview scan was performed in a region of neuropil in the CA1 region of an organotypic hippocampal slice. Next, the central 5 x 5 x 2.5 μm^3 volume was exposed to STED in 20 consecutive volumetric scans in *xzy*-scan mode with 70 μs voxel dwell time for long-exposure STED and 10 μs for LIONESS datasets. Excitation and STED power were identical and corresponded to the parameters used in LIONESS imaging, with 90 mW STED power at 80/20 distribution between phase patterns. 10 min after the last volume was acquired, a second 70 x 70 μm confocal overview scan was done of the same region and plane as in the initial measurement.

For long-term repeated imaging of hippocampal neuropil (**Suppl. Fig. 15**), the sample was mounted and placed on the microscope as described in the section on LIONESS imaging. For the first 4 acquisitions within 1h, the sample was kept in place, with the imaging media (carbogenized ACSF with 150 μM Atto 643) exchanged after 30 min. After that, the sample was placed back onto cell culture inserts and into the tissue culture incubator at 37 °C and 5% CO₂ until the next imaging session one day later. The same procedure was repeated for the last imaging time point after 3 days.

For long-term repeated imaging of chemogenetically activated mossy fibre boutons (Fig. 5), the sample was placed back after the first imaging session onto cell culture inserts and incubated at 37 °C and 5% CO₂. Media was changed after 45 min to wash out residual CNO, and the sample was placed into the tissue culture incubator until the second imaging session on the next day.

PSD95-HaloTag labelling

Organotypic hippocampal brain slices of PSD95-HaloTag mice were live labelled using Janelia Fluor (JF)585-HaloTag ligand (Janelia). The fluorescent ligand was dissolved in anhydrous DMSO to a stock concentration of 500 μM , aliquoted and stored at -20°C. Before imaging, the fluorescent ligand was added to the culture medium to a final concentration of 500 nM (1:1000) and incubated for at least 45 min at 37 °C.

Viral vector assembly and synaptophysin labelling

Preparation of AAV and RVdG_{envA}-CVS-N2c vectors has previously been described.^{42,54} Briefly, AAV2-CaMKIIa-TVA-2A-N2cG (Addgene #172363) vectors were pseudotyped with the AAVdj capsid protein by co-transfection of HEK293T cells. Three days later, the cells were harvested and lysed, and the viral stock was purified using heparin-agarose affinity binding. RVdG_{envA}-CVS-N2c-nl.EGFP-SypEGFP (Addgene #172380) were rescued using HEK-GT cells and then amplified and pseudotyped using BHK-eT cells. Viral vectors were purified and concentrated from the supernatant using ultracentrifugation and resuspended in PBS.

For live labelling of synaptic vesicles, first AAV-CaMKIIa-TVA-2A-N2cG was added to organotypic hippocampal slice cultures at 7-10 days in vitro (DIV) for dual expression of the TVA avian receptor and the rabies N2c glycoprotein (N2cG). 14 days later, envA-pseudotyped, G-deleted CVS-N2c rabies viral particles were added for expression of a synaptophysin-EGFP fusion protein and additional EGFP expression in the cell nucleus (RVdG(envA)-CVS-N2c-nlGFP-sypGFP). 4-5 days after addition of the rabies vectors, EGFP expression was strong enough for imaging.

Myelin labelling

Live labelling of myelin was performed using FluoroMyelin™ Green (ThermoFisher Scientific, #F34651). The dye was diluted 1:300 in culture media for organotypic hippocampal slices and incubated with the sample at 37 °C for at least 30 min before imaging.

Calcium imaging

Cultured organotypic hippocampal slices of Prox1-cre/Ai95 (GCaMP6s) mice shown in **Suppl. Fig. 16** were ECS labelled for LIONESS imaging as described above. To reduce level of inhibition, 10 μM GABA_A receptor antagonist gabazine were added to the imaging media at the start of the imaging session. A region of interest was first repeatedly imaged via confocal scanning (488 nm excitation, 1.1 μW) of an individual plane with 50 x 50 nm² pixel size and 5 μs pixel dwell (frame rate ~1.25 Hz) to detect GCaMP signals. After recording, the enclosing volume was scanned in LIONESS mode. The GCaMP recording was overlaid with a corresponding plane of the volumetric LIONESS acquisition in **Suppl. Fig. 16c**. The same volume was imaged a second time 10 min after the first acquisition. The sample was kept in place in between the two recordings.

Chemogenetic activation with calcium imaging

Chemically targeted activation with simultaneous calcium imaging of neurons was done using AAVs containing a Cre-dependent DREADD⁵⁵ construct (AAV-DIO-CAG-hM3Dq-2A-dTomato; plasmid available from the authors upon request) added to organotypic hippocampal slice cultures of Prox1-cre/Ai95 (GCaMP6s) mice at DIV 4-6. Each transduced cell expressed both cytoplasmic dTomato and the excitatory designer receptor hM3Dq. Concentrated viral stock (7×10^{11} GC/ml) was first diluted 1:10 in culture medium, and subsequently 5 μ l were carefully placed on top of each slice. Weak fluorescence was already detectable \sim 3 days after transfection and live-imaging was performed from day 9 onwards after viral transduction. To activate the designer receptor, Clozapine-N-oxide (CNO) was added (3 μ M final concentration) to the imaging medium (fluorophore containing ACSF). The GCaMP signal was recorded via confocal scanning (488 nm excitation, 3.9 μ W) of an individual plane using a pixel size of 100 x 100 nm² and dwell time of 20 μ s, which resulted in a frame rate of \sim 2 Hz. The GCaMP recording together with the dTomato signal were overlaid with a corresponding plane of the LIONESS acquisition for representation.

Electrophysiology

Organotypic slice cultures were submerged in artificial cerebrospinal fluid (ACSF) containing 125 mM NaCl, 25 mM NaHCO₃, 25 mM D-glucose, 2.5 mM KCl, 1.25 mM NaH₂PO₄, 2 mM CaCl₂, and 1 mM MgCl₂, with pH maintained at 7.3, equilibrated with a 95% O₂/5% CO₂ gas mixture at \sim 22 °C (room temperature). Glass micropipettes were pulled from thick-walled borosilicate glass (2 mm O.D., 1 mm I.D.) and filled with intracellular solution containing 135 mM K-gluconate, 20 mM KCl, 0.1 mM EGTA, 2 mM MgCl₂, 4 mM Na₂ATP, 0.3 mM GTP, 10 mM HEPES, with the addition of 20 μ M AlexaFluor488 hydrazide and 0.2 % (w/v) biocytin as required. Pipettes were positioned using two LN mini 25 micromanipulators (Luigs and Neumann) under visual control on a modified Olympus BX51 microscope equipped with a 60x water-immersion objective (LUMPlan FI/IR, NA = 0.90, Olympus, 2.05 mm working distance). Two neurons were simultaneously recorded in the whole-cell patch-clamp configuration, with signals acquired on a Multiclamp 700B amplifier (Molecular Devices), low pass filtered at 6 kHz and digitized at 20 kHz with a Cambridge Electronic Design 1401 mkII AD/DA converter. Signals were acquired using Signal 6.0 software (CED). Action potential phenotypes were recorded on sequential current pulse injections (-100 to +400 pA) in the

current clamp configuration. Neurons were identified based on morphological and action potential phenotypes. In current clamp recordings, pipette capacitance was 70 % compensated. Synaptic connectivity was assessed by sequential current injection into either recorded cell in the current-clamp configuration, while recording EPSCs (Excitatory Postsynaptic Currents) from the other in the voltage-clamp configuration. Presynaptic action potentials were elicited by five 1-2 nA current injection pulses for 2-3 ms at 20 Hz. Putative monosynaptic connections were identified by EPSC generation (peak current > 2.5 times the standard deviation of baseline noise) in the postsynaptic cell with short latency (< 4 ms) from the presynaptic action potential peak. Recordings were analysed using Stimfit⁵⁶ and MATLAB-based scripts. After recording, neurons were resealed by forming an outside-out patch on pipette retraction, before immersion in solutions for live imaging.

SulfoAtto 643 synthesis and characterization

In a round bottom flask equipped with a magnetic stir bar, Atto 643 NHS-ester (ATTO-TEC: #AD 643-35; 5.0 mg, 5.23 μ mol, 1.0 equiv.) was dissolved in a mixture of DMF:dH₂O (700:300 μ L). DIPEA (6.9 mg, 53.8 μ mol, 10 equiv.) and taurine (3.4 mg, 26.8 μ mol, 5.0 equiv.) were added successively and the reaction mixture was allowed to incubate for 60 min before it was quenched by the addition of acetic acid (10 μ L). Semi-preparative RP-HPLC was performed on an Agilent 1260 Infinity II LC System equipped with columns Reprospher 100 C18 columns (5 μ m: 250 x 10 mm at 4 mL/min flow rate. Eluents A (0.1% TFA in H₂O) and B (0.1% TFA in MeCN) were applied as a linear gradient (MeCN:H₂O+0.1% TFA = 10:90 to 90:10 over 50 minutes). Peak detection and collection were performed at λ = 650 nm and provided 4.5 mg (4.7 μ mol) of the desired product as a blue powder after lyophilization in 91% yield. Characterization was done using liquid chromatography – mass spectrometry. It was performed on an Agilent 1260 Infinity II LC System equipped with Agilent SB-C18 column (1.8 μ m, 2.1 x 50 mm). Buffer A: 0.1% FA in H₂O Buffer B: 0.1% FA acetonitrile. The gradient was from 10% B for 0.5 min \rightarrow gradient to 95% B over 5 min \rightarrow 95% B for 0.5 min \rightarrow gradient to 99% B over 1 min with 0.8 mL/min flow. Retention times (t_R) are given in minutes (min).

Restoration network training

Volumetric paired low-exposure, low-SNR training input data and high-exposure, high-SNR “ground truth” data were recorded in a voxel-exact mode by collecting low-SNR data during the first 10 μ s voxel dwell time and additional photons during the remaining 60 μ s dwell time. High-SNR ground truth for network training were thus generated by adding up counts from the total 70 μ s dwell time in FIJI Version: 2.3.0/1.53f (Fiji/process/calculator plus/add). Other

imaging parameters were as described in the section “LIONESS imaging” (2.9 μ W (640 nm) excitation laser power, 90 mW STED laser power with power ratio of z-STED/xy(4 π)-STED of 80/20, voxel size 50 x 50 x 50 nm³). 76 volume pairs of 12.5 x 12.5 x 5 μ m each were used for training. Network training (Version: CSBDeep 0.6.1)²⁸ parameters were as follows: 3D mode, 32 x 32 x 32 pixel patch size, 190 patches per volume, 150 steps per epoch, 150 epochs, batch size 32, and training data was loaded as 16-bit TIFF files. Software was installed from GitHub (<https://github.com/CSBDeep/CSBDeep>). A workstation with the following hardware components was used: Intel® Xeon® W “Skylake” W-2145, 3.60 GHz processor, 128 GB RAM, NVIDIA GeForce RTX 2080Ti graphics card.

Denoising

To denoise confocal images recorded simultaneously with the LIONESS data in **Fig. 4** and **Suppl. Fig. 6** and **14b**, Noise2void⁵⁷ (Version 0.2.1) was applied to individual channels with the following parameters: noise2void 3D mode, patch size 32 x 32 x 32 pixels, each patch augmented with rotations and axis-mirroring, training steps per epoch 150, number of epochs 75 (SYP1-EGFP) or 100 (PSD95-HaloTag), batch size 16 (SYP1-EGFP) or 32 (PSD95-HaloTag). Software was installed from GitHub (<https://github.com/juglab/n2v>). A workstation with the following hardware components was used: Intel® Xeon® W “Skylake” W-2145, 3.60 GHz processor, 128 GB RAM, NVIDIA GeForce RTX 2080Ti graphics card.

Volume extension

For stitching of volumetric images, the Fiji 3D stitcher was used (Fiji/Plugins/deprecated/3D Stitching; linear blending, fusion alpha 2.0).

Manual segmentation and proofreading

Planes for manual segmentation were first upscaled 5-fold without interpolation (plane depth was kept at original 50 nm spacing). Segmentation itself was done using VAST⁵⁸ 1.3.0. and 1.4.0. Software was downloaded from <https://lichtman.rc.fas.harvard.edu/vast/>. For proofreading of automated segmentations data was visualized using Neuroglancer (<https://github.com/google/neuroglancer>) and corrected using VAST 1.4.0.

Segmentation

We based our implementation of the automatic segmentation pipeline on the *pytorch_connectomics*^{34,35} framework. We used a U-Net architecture and trained the neural network to produce affinity maps which were then processed by a watershed algorithm to obtain the final segmentations.

During training, the U-Net required volume data and the corresponding manual ground-truth segmentation. First, in order to adapt the input datasets to the framework requirements and maximize its performance, we applied a pre-processing step converting the volume data to 8-bit format and stretching the intensity to cover the whole intensity range. Then, the pre-processed volumes together with the corresponding ground-truth segmentations were passed into the U-Net. Three key parameters during training were the sample size, the number of training iterations and the data augmentation. Given the anisotropic step size (5-fold upsampling in the *xz*- or *yz*-plane for manual segmentation) of the input volume we noticed that using a sample size of [128 x 128 x 64], with the lowest number corresponding to the non-upsampled axis, significantly improved the performance of the neural network. We increased the number of training iterations from the default 100k to 500k which further helped reduce segmentation errors. We found this number of iterations to be a reasonable compromise between training time and inference performance. Finally, we enabled all available data-augmentation techniques.

During inference, we passed the pre-processed volume data into the U-Net and obtained the affinity map as output. At inference time we used the same sample size used during training, with appropriate padding if the input volume was small, and test-time augmentation via axis-mirroring. The values in the final affinity map corresponded to the mean of the values obtained for each augmented case. The output affinity map was processed using the watershed algorithm to produce the labelled automatic segmentation. Our pipeline combined two different watershed implementations. First, we applied the image-based watershed method⁵⁹ (<https://github.com/zudi-lin/zwatershed>) on each slice to compute fragment masks. These were then passed to a volume-based implementation (<https://github.com/zudi-lin/waterz>), which was applied on the affinity map, producing the final segmentation. We used watershed thresholds in the range [0.2-0.4] to minimize oversegmentation but also avoid merges, which tend to be more tedious to fix during proof-reading. The resulting segmentations contained spurious segments, which we cleaned during a final post-processing step by removing those that consisted of too few voxels (fewer than 10) or slices (fewer than 2). This last step significantly

facilitated later proof-reading. The resulting segmentations were then analysed visually, using Neuroglancer, and quantitatively, using metrics such as segment size distribution and split ratio of ground truth segments with respect to automatic segmentations.

We trained the U-Net on a 8-GPU (Nvidia 3090s) node, using 32 CPUs and 128 GB RAM during 500k iterations, which took 6 days. Inference time falls in the 10 to 40 minutes range, depending on the size of the input volume, and can be performed on a more modest compute node. In our case, we used a 2-GPU (Nvidia 3090s) node using 8 CPUs. The post-inference watershed and segmentation cleaning operations were performed on the inference node and took 10 minutes to 20 minutes to complete.

Visualization

3D visualizations were done either using VAST⁵⁸ 1.4.0. (**Fig. 1a, 2a** and **Suppl. Fig. 7, 8a, 11, 12, 19a**), Neuroglancer (**Fig. 3b, 4b, 5b, Suppl. Fig. 9, 10, 18, 19b**), Blender 2.93.4 (**Fig 1a, 3c, Suppl. Fig. 8b**) or Neuromorph⁶⁰ 2.8 (**Fig. 3e**). Blender-generated visualizations were produced based on 3D meshes extracted from segmentations using marching cubes (as implemented in Scikit-Image). These 3D meshes were first smoothed in Blender using a vertex-based smoothing operation that flattens angles of mesh vertices and finally the scene was rendered using Blender's Cycles rendering engine. The schematics in the upper row of **Fig. 1a** were created with Biorender.com.

Dendrite abstraction

For representing dendrite synaptic connectivity in **Fig. 3e**, we developed a visual spine analysis approach inspired by Barrio⁶¹, a software for visual neighbourhood analysis of nanoscale neuronal structures. We computed surface meshes for all axons and dendrites based on the segmented neuronal structures. Next, we used Neuromorph⁶⁰ to compute spine lengths by specifying the base and tip of each spine and plotted spine positions and relative spine length according to position on the dendrite. Spine lengths were computed between the base and tip of each spine, following the spine's central axis (skeleton). We abstracted the complex 3D morphology and connectivity of a dendrite from 3D to 2D to reduce visual clutter, while preserving relative spine positions and spine lengths. To do so, we mapped a dendrite's 3D skeleton structure to a simplified, but topologically correct, 2D representation. We preserved all relative distance relations within a dendrite (i.e., distances between spines), and encoded

spine length at each spine location. Spine lengths were represented as bars, scaled relatively to the largest spine length of the dendrite.

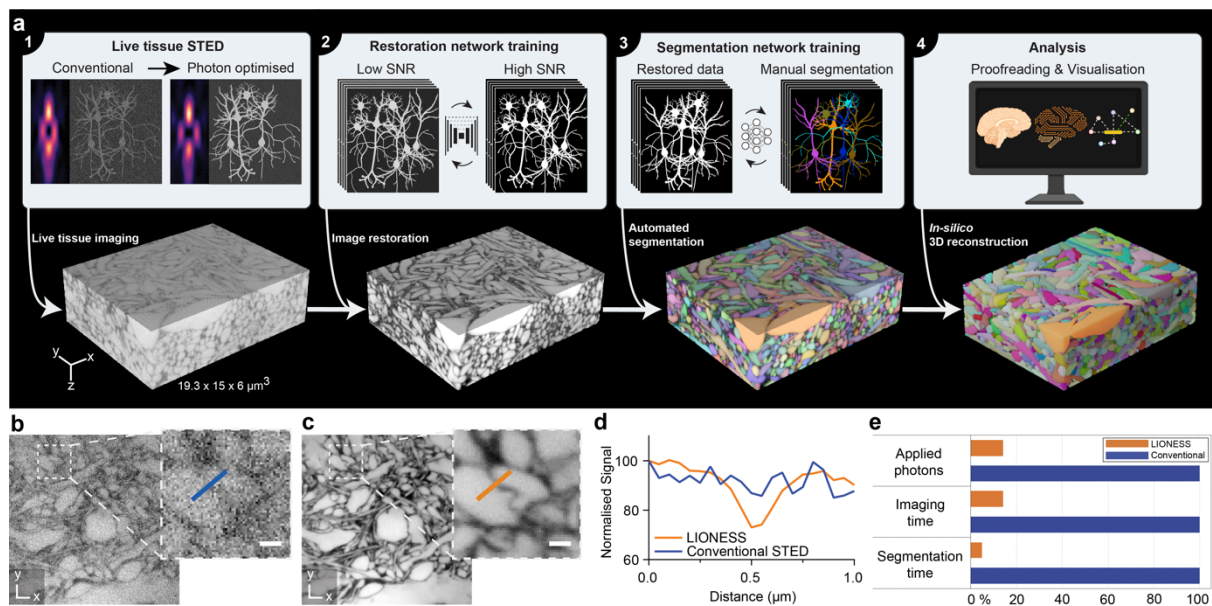


Fig. 1: LIONESS enables saturated reconstruction of living brain tissue.

a, Integrated imaging and analysis pipeline, exemplified for a volume of a living human brain organoid. LIONESS includes tissue-optimized, high-speed, low-exposure volumetric imaging of extracellularly labelled living brain tissue at isotropic super-resolution and two-step, deep-learning-based signal-to-noise ratio (SNR)-restoration and segmentation. Imaging optimizations, deep-learning training, and analysis (top) flowing into individual processing steps (bottom): (1) Infrared STED with tissue-adapted light patterns for improved spatial distribution of on/off contrast. (2) Training of neural network on paired low-exposure, low-SNR and high-exposure, high-SNR isotropically super-resolved volumes for high effective SNR at reduced photon load. (3) Training of neural network for 3D-segmentation of cellular structures with manually annotated volumetric data. (4) Postprocessing with proofreading and data visualization/interpretation. **b,c,d** Improvement of feature definition with LIONESS at constant live-tissue compatible STED light exposure in living hippocampal brain tissue. Single planes of isotropically super-resolved tissue. Scale bars, magnified views: 500 nm. **b**, Conventional STED imaging with 2π -helical and π -tophat phase modulation patterns for lateral (xy)- and axial (z)-resolution increase, respectively. **c**, Same region imaged with tissue-adapted STED patterns (4π -helical and π -tophat modulation), improved detector dynamic range (allowing doubled excitation power), and deep-learning based SNR-restoration. STED power and dwell time were identical as in panel **b**. **d**, Line profiles across a synaptic cleft as indicated in panels **b** and **c**. **e**, Light exposure and imaging time are reduced by 86% with LIONESS imaging parameters compared to high-photon load ground truth, in addition to the SNR improvement from optical optimizations (step 1 in panel **a**). Deep-learning accelerates segmentation by several orders of magnitude whereas gain in total segmentation speed, including proofreading, also depends on sample complexity. Lookup tables for LIONESS are linear and inverted throughout, i.e. ranging from black (maximum photon counts of extracellular label) to white (minimum counts within cells).

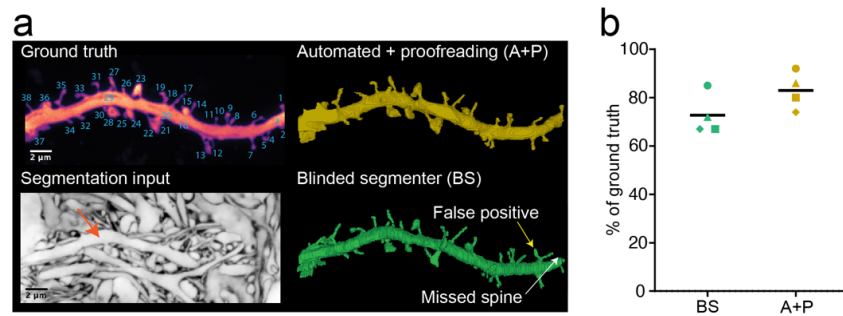


Fig. 2: Validation of segmentation.

a, Top left: Maximum intensity projection of a hippocampal dendrite positively labelled by cytosolic EGFP expression with numbered spines, serving as ground truth for segmentation.

Bottom left: Plane from volumetric LIONESS acquisition with arrow indicating the same dendrite. Top right: 3D-reconstruction after automated segmentation and proofreading by the experimenter who recorded the data (A+P). As this person was not blinded to the EGFP-channel, this serves to indicate which spines can be retrieved from LIONESS but not as independent control. Bottom right: Fully manual spine detection by a segmenter blinded to the EGFP-channel (BS). Exemplary missed and false positive spines are indicated by yellow and white arrows, respectively. LIONESS image is a maximum intensity projection spanning 150 nm. **b**, Quantification of detected spines from the automated + proofreading (A+P, orange) and manual (BS, green) segmentation as a fraction of positively labelled ground truth. Correctly assigned spines were counted as +1, false positives as -1 and the sum normalized to the total number of spines in the positively labelled ground truth.

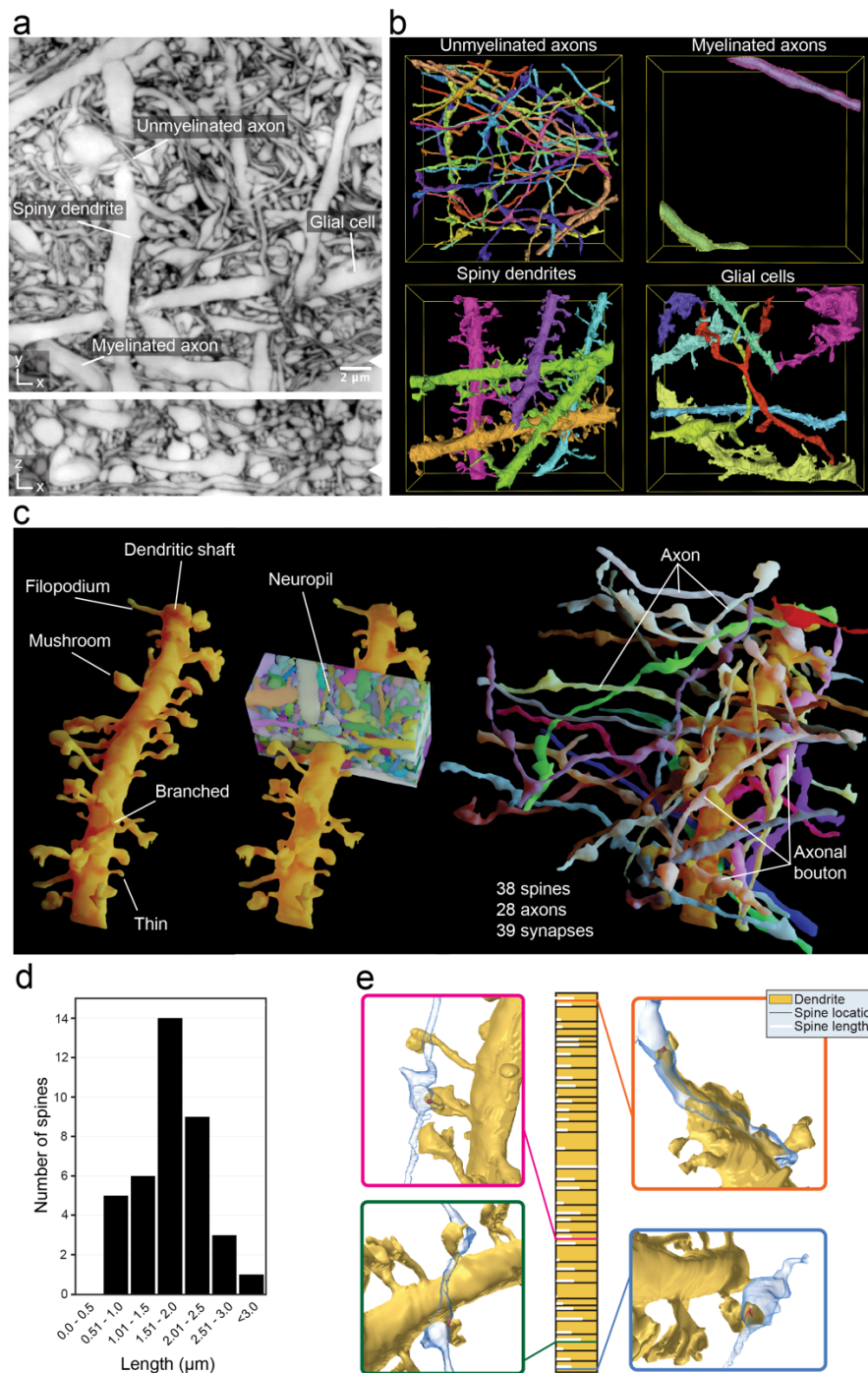


Fig. 3: Connectivity reconstruction in live hippocampus.

a, Orthogonal planes from a LIONESS volume in xy - and xz -directions in hippocampal neuropil. Arrowheads indicate position of corresponding orthogonal planes. Scale bar: 2 μm . LIONESS images are maximum intensity projections spanning 150 nm. **b**, 3D-reconstructions of exemplary cellular structures extracted from panel a. **c**, 3D-reconstruction of a dendrite from panel a, showing various spine shapes (left), its embedding in dense neuropil (middle) and the 28 axons making a total of 39 synaptic connections at 38 spines (right). **d**, Distribution of spine lengths on the dendrite shown in panel c. **e**, Spine location (black bars) and relative spine lengths (white bars) along the dendrite (gold) with 3D-renderings of exemplary synaptic connections.

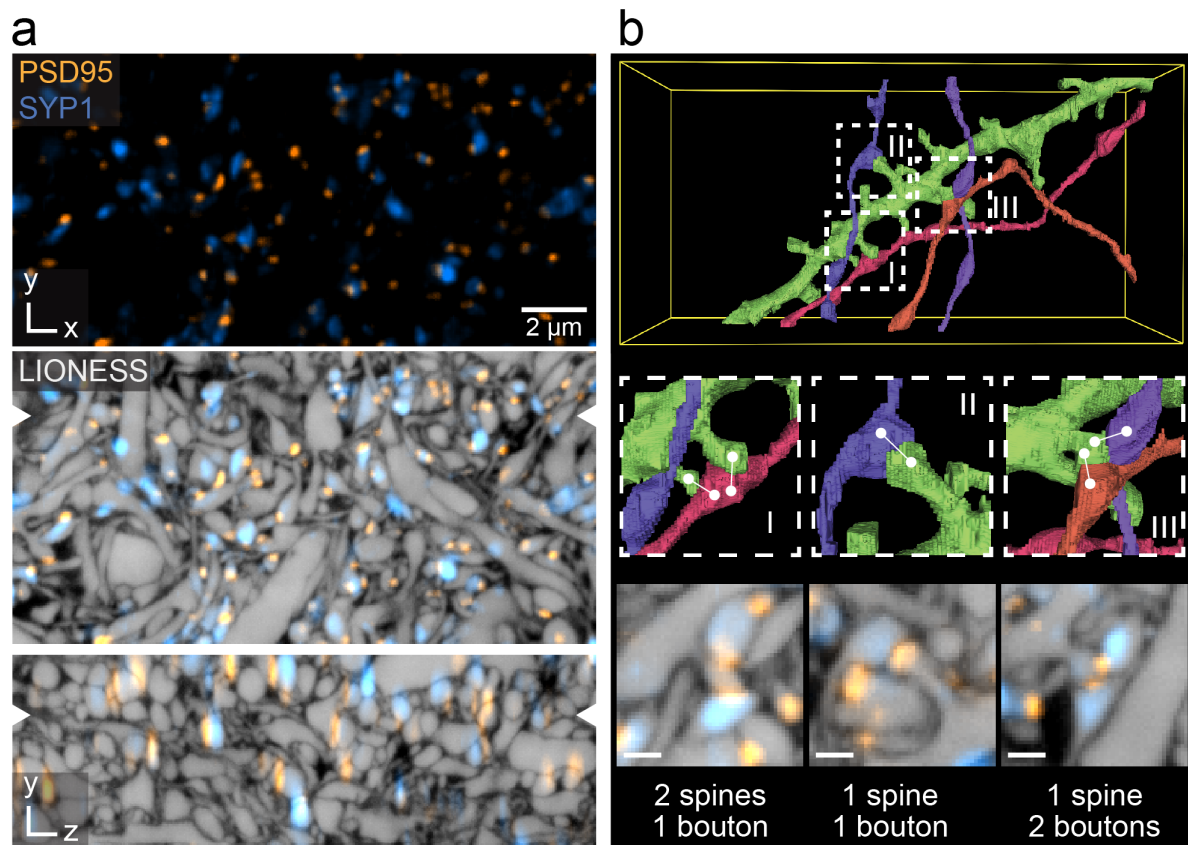


Fig. 4: Molecularly informed tissue reconstruction.

a, Single orthogonal planes from a LIONESS volume in xy - and xz -directions in hippocampal CA1 neuropil with synaptophysin 1 (SYP1, blue) and postsynaptic density protein 95 (PSD95, orange) live-labelled to molecularly define pre- and post-synapses, respectively. Top: Confocal image of molecular markers after denoising. Middle, bottom: Overlay with isotropically super-resolved LIONESS data, clarifying the relationship of molecularly defined pre- and postsynapses. SYP1 labelling of synaptic vesicles was done with a pseudotyped rabies virus, such that a subset of synapses were highlighted, whereas transgenic PSD95-HaloTag expression is expected to label all excitatory post-synapses. SYP1 and PSD95 signals were recorded in diffraction-limited mode and hence extend beyond the cellular structures defined by LIONESS. Arrowheads indicate position of corresponding orthogonal planes. Scale bar: 2 μm. Images are maximum intensity projections spanning 150 nm. **b**, 3D-reconstruction of a selected dendrite (green) from the LIONESS volume in panel a with 4 synaptically connected axons (upper image). Dashed boxes indicate positions of magnified views highlighting diverse geometric arrangements of boutons and spines (middle panels). White lines indicate synaptic connections retrieved from the molecular information overlaid with LIONESS data (lower panels). Scale bars: 500 nm.

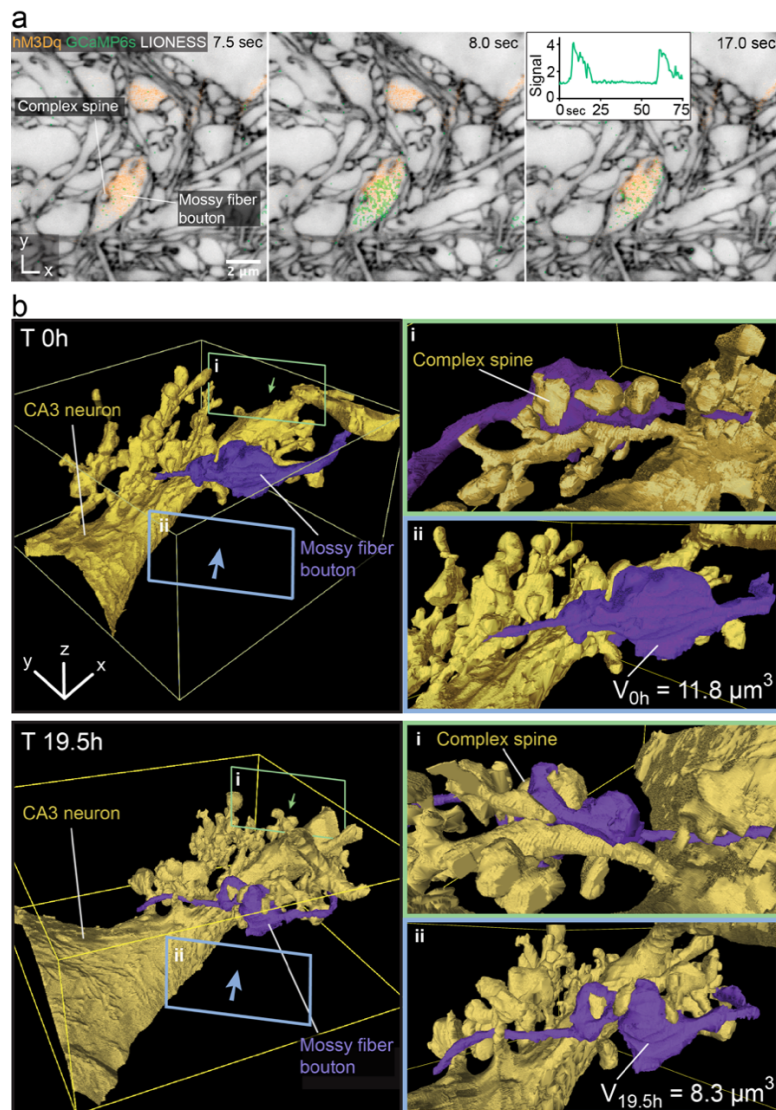
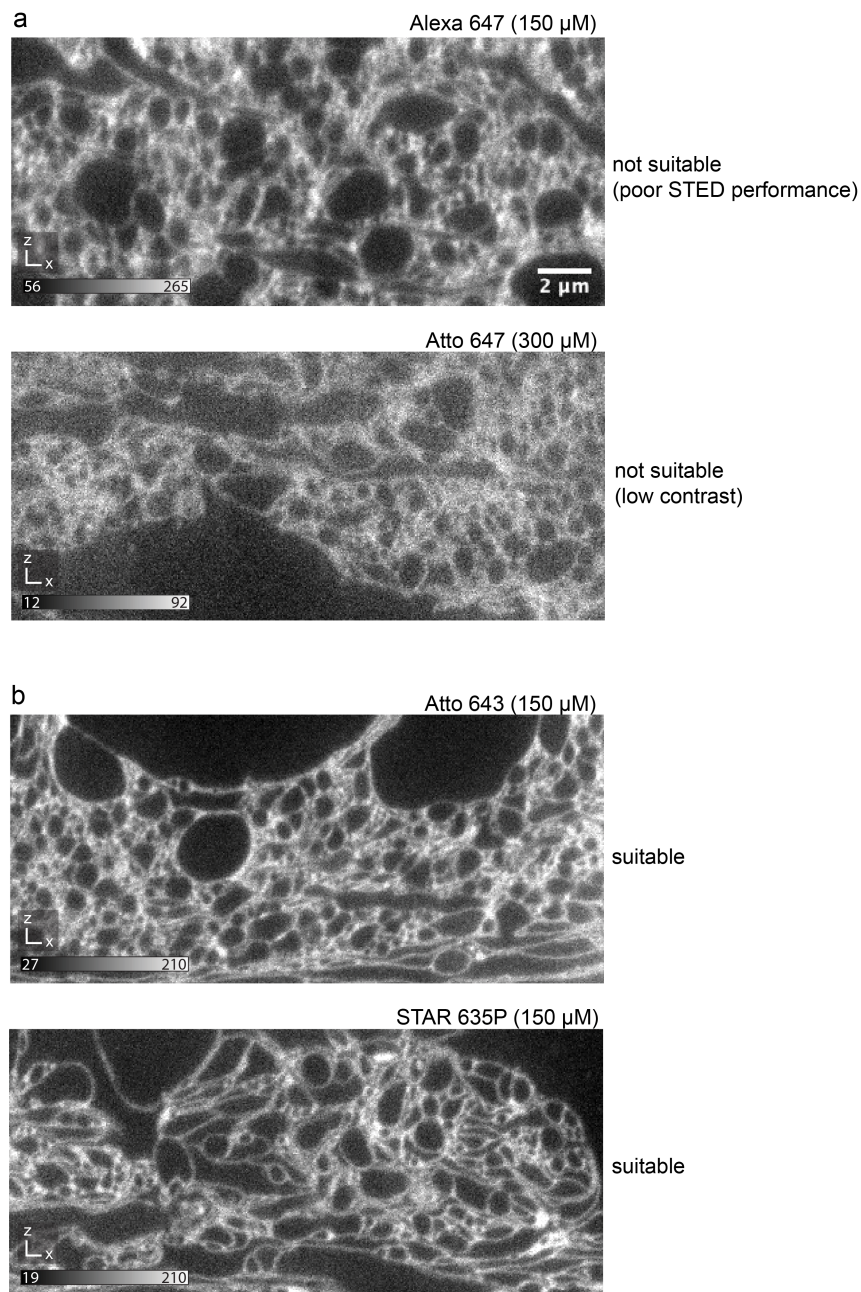


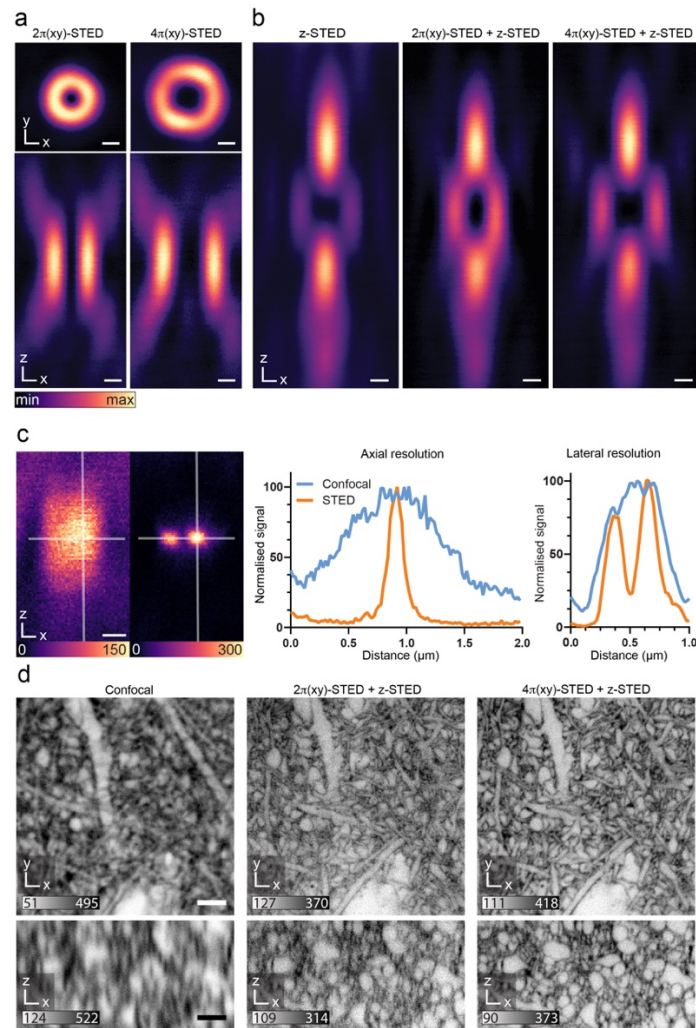
Fig. 5: 3D-morphodynamics and chemogenetically induced Ca^{2+} -activity in hippocampal mossy fibre-CA3 pyramidal neuron synapses.

a, Single plane of a LIONESS volume where a subset of mossy fibre boutons expressed both the excitatory DREADD (designer receptor exclusively activated by designer drug) hM3Dq (coupled with dTomato, orange) and the calcium indicator GCaMP6s (green). LIONESS and hM3Dq images are identical replicates placing the overlaid time-varying Ca^{2+} -signals after stimulation with the DREADD ligand CNO into structural context, with 3 example points from a time series. The insert in the top right shows GCaMP signal (averaged pixel value) of the whole series as a function of time. LIONESS image is a maximum intensity projection spanning 150 nm. Scale bar: 2 μm . **b**, 3D-reconstructions of a hM3Dq-expressing mossy fibre bouton (purple) and its postsynaptic partner, a CA3 pyramidal neuron (gold) with complex spines at two timepoints (top: 0h, bottom: 19.5h). V_{0h} and $V_{19.5h}$ are bouton volumes at the respective time points. Green (i) and blue (ii) frames indicate the viewing angles from opposite directions for the magnified views on the right. The structures designated by the lettering refer to the same bouton and complex spine in both panels.



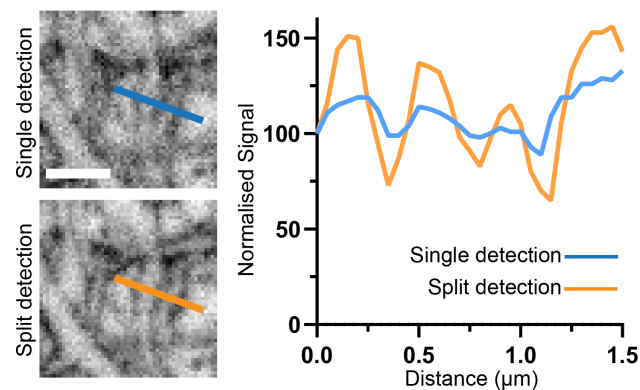
Supplementary Fig. 1

Fluorophore screening. **a**, Two examples of fluorophores yielding insufficient delineation of fine cellular structures, due to suboptimal STED performance (top) or poor extra- vs. intracellular contrast (bottom). **b**, Two examples of fluorophores with high STED performance and high extra- vs. intracellular contrast (Atto 643, Abberior STAR 635P), yielding adequate delineation of fine cellular structures. All images show raw *xz*-planes recorded with tissue-optimized STED with near-isotropic resolution. Fluorophores applied at indicated concentrations to ECS in organotypic hippocampal slices. The custom synthesized sulfonated variant of Atto 643 (SulfoAtto 643) was equally suited and used interchangeably with Atto 643. Scale bar: 2 μ m.



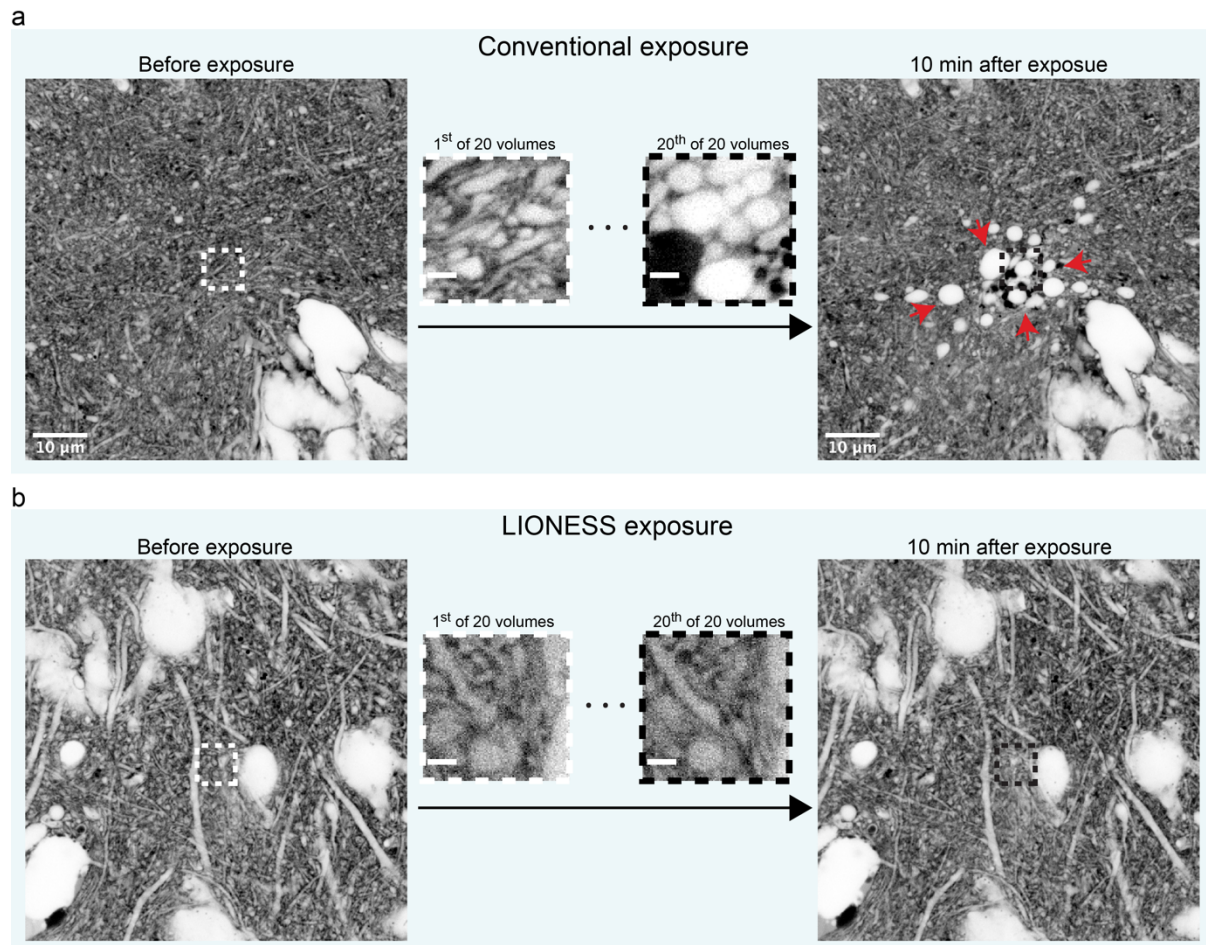
Supplementary Fig. 2

Tissue-optimized STED. **a,b**, STED light intensity distributions in the focal region. **a**, Lateral (top) and axial (bottom) sections for 2π - and 4π -helical phase modulation. Scale bars: 250 nm. **b**, Axial sections of the π -tophat phase modulated z-STED pattern (left), an incoherent superposition of $2\pi(xy)$ - and z-STED patterns (middle), and of $4\pi(xy)$ - and z-STED patterns (right). Power distribution between the z- and xy-STED patterns in the superpositions was 80% vs. 20%. Scale bars: 250 nm. **c**, Axial scan of 40 nm diameter fluorescent beads in confocal mode (left) and with STED employing combined $4\pi(xy)$ - and z-STED patterns (right). Scale bar: 250 nm. Profiles along the lines in lateral and axial directions as indicated in the images. **d**, Extracellularly labelled neuropil in organotypic hippocampal slices. Orthogonal planes in xy- and xz-direction for diffraction-limited confocal (left), classical 2π -helical and π -tophat phase modulation for lateral and predominantly axial resolution increase, respectively (middle), and combination of 4π -helical plus π -tophat modulation for isotropic resolution with improved quenching of excitation outside the central STED intensity minimum. The double helicity pattern facilitates robust in-tissue co-alignment of intensity minima. Scale bar: 2 μ m. Raw data with linear, inverted colour scale.



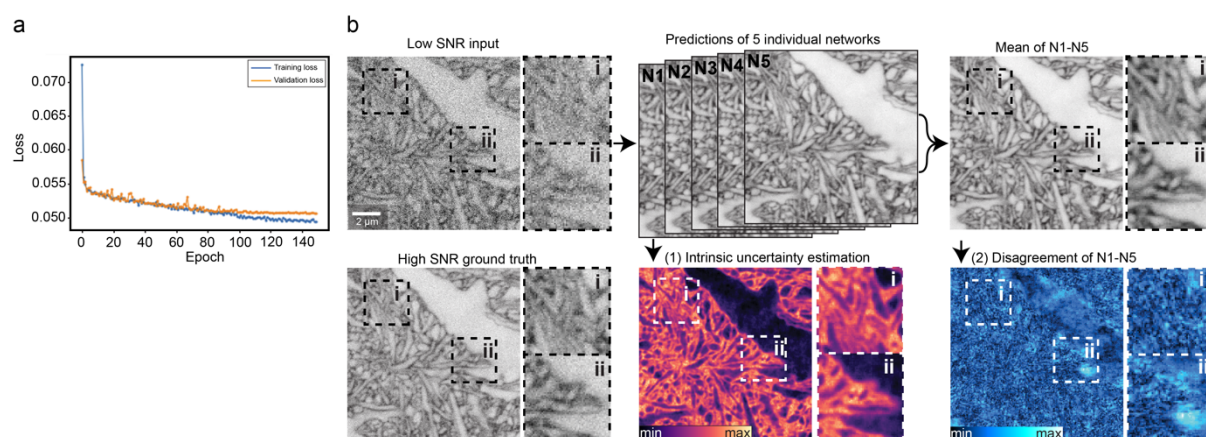
Supplementary Fig. 3

Detector dynamic range. Same region imaged with a single detector (top) or with a split detection path and two single-photon counting avalanche photodiodes as detectors (bottom). Line profiles over corresponding structures for single (blue) and split (orange) detection. STED power and pixel dwell times were identical, 4π -helical and π -tophat phase modulation patterns were applied for STED. Increased detector dynamic range allowed higher excitation power within the linear detection regime. Single imaging planes. Scale bar: 1 μm .



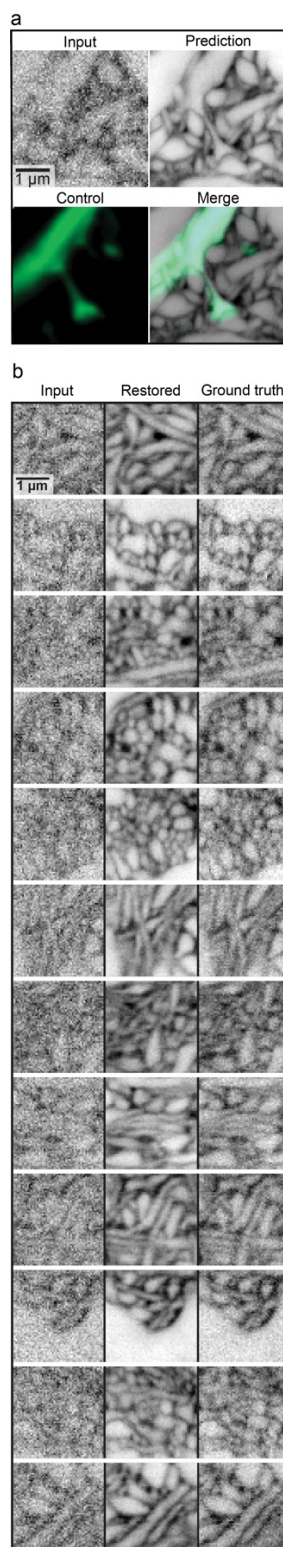
Supplementary Fig. 4

Live-tissue compatibility. **a**, Confocal overview images before (left) and 10 minutes after (right) scanning the same volume ($5 \times 5 \times 2.5 \mu\text{m}^3$) in high-photon load STED mode ($70 \mu\text{s}$ voxel integration time). Central images are single planes of the first and last STED volume acquired. Red arrows indicate blebbing and disintegrating cells. **b**, Confocal overview images before (left) and 10 minutes after (right) scanning the same volume ($5 \times 5 \times 2.5 \mu\text{m}^3$) using LIONESS parameters ($10 \mu\text{s}$ voxel integration time). Central images are single planes of the first and last LIONESS volume acquired. Scale bars: confocal: $10 \mu\text{m}$, STED: $1 \mu\text{m}$.



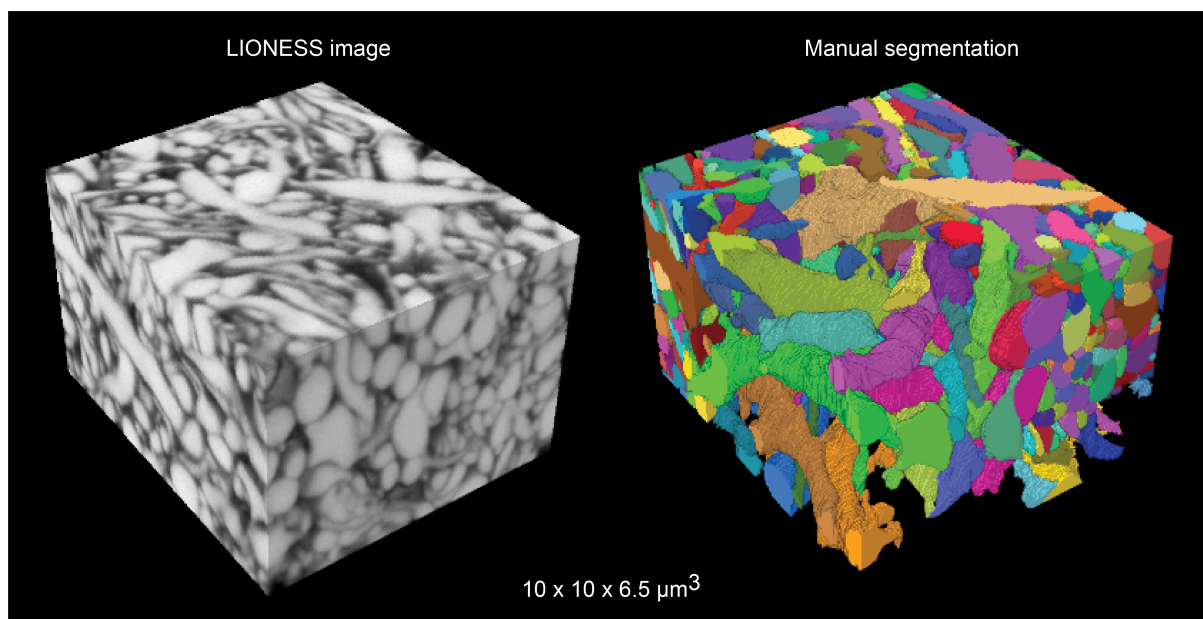
Supplementary Fig. 5

SNR restoration training. **a**, Training and validation loss as a function of epoch number of the SNR-restoring network. **b**, Validation of network predictions from paired low- and high-SNR data that were not part of the network training, recorded with tissue-optimized STED in extracellularly labelled hippocampal tissue. (1) Intrinsic probabilistic estimation of uncertainty for individual predictions (lower panel, middle) and (2) standard deviation of the mean (disagreement) of 5 trained networks N1-N5 for each voxel (lower panel, right). Raw data and network predictions are maximum intensity projections spanning 150 nm.



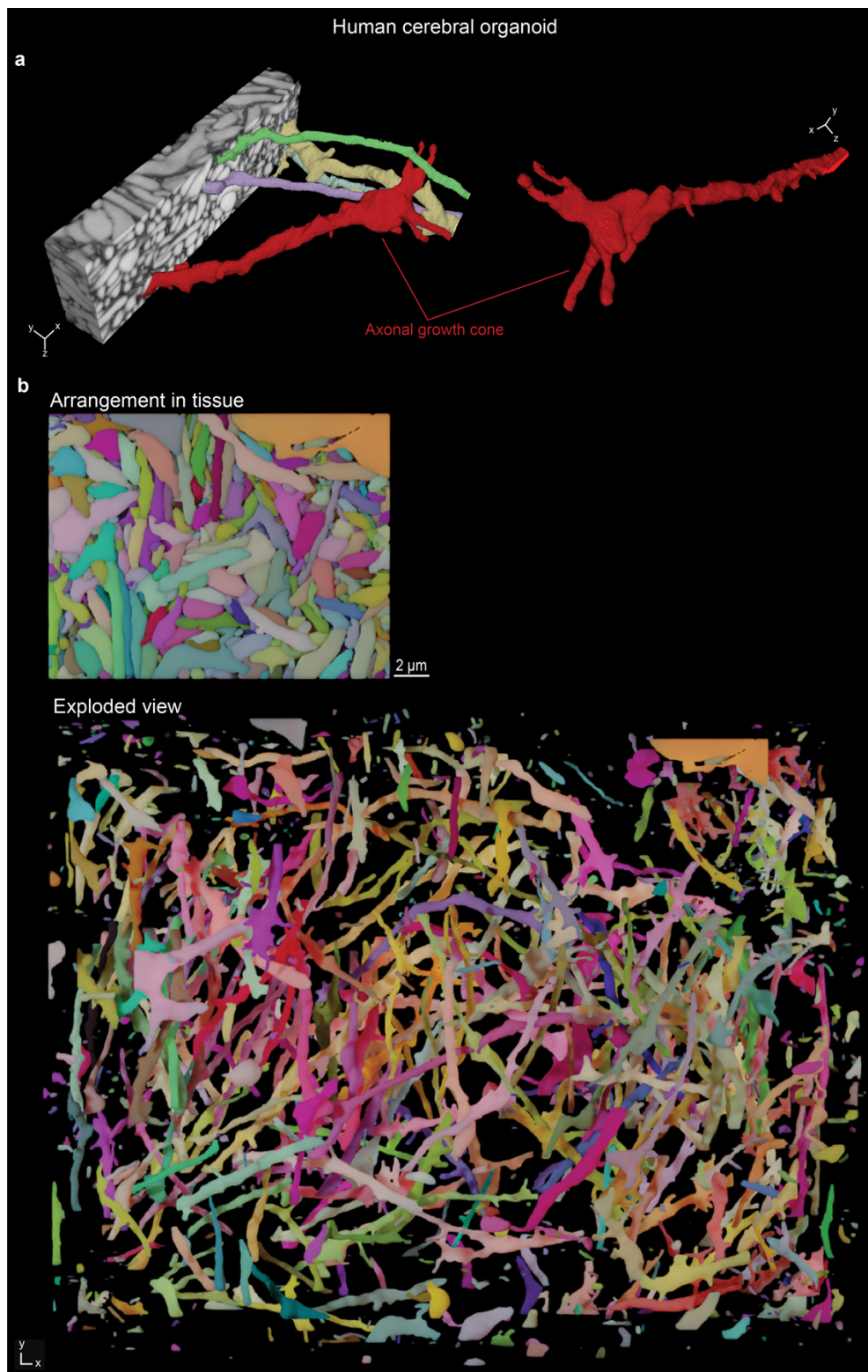
Supplementary Fig. 6

Validation of SNR restoration. **a**, Raw low-exposure input, SNR-restored network prediction, positively labelled (Thy1-EGFP) control, and overlay of prediction and control. **b**, Twelve exemplary areas of raw input, SNR-restored network prediction, and high-SNR ground truth. Scale bars: 1 µm. Images except for positively labelled control displayed with inverted look-up table. Maximum intensity projections spanning 150 nm. Data used in validation were not part of restoration network training.



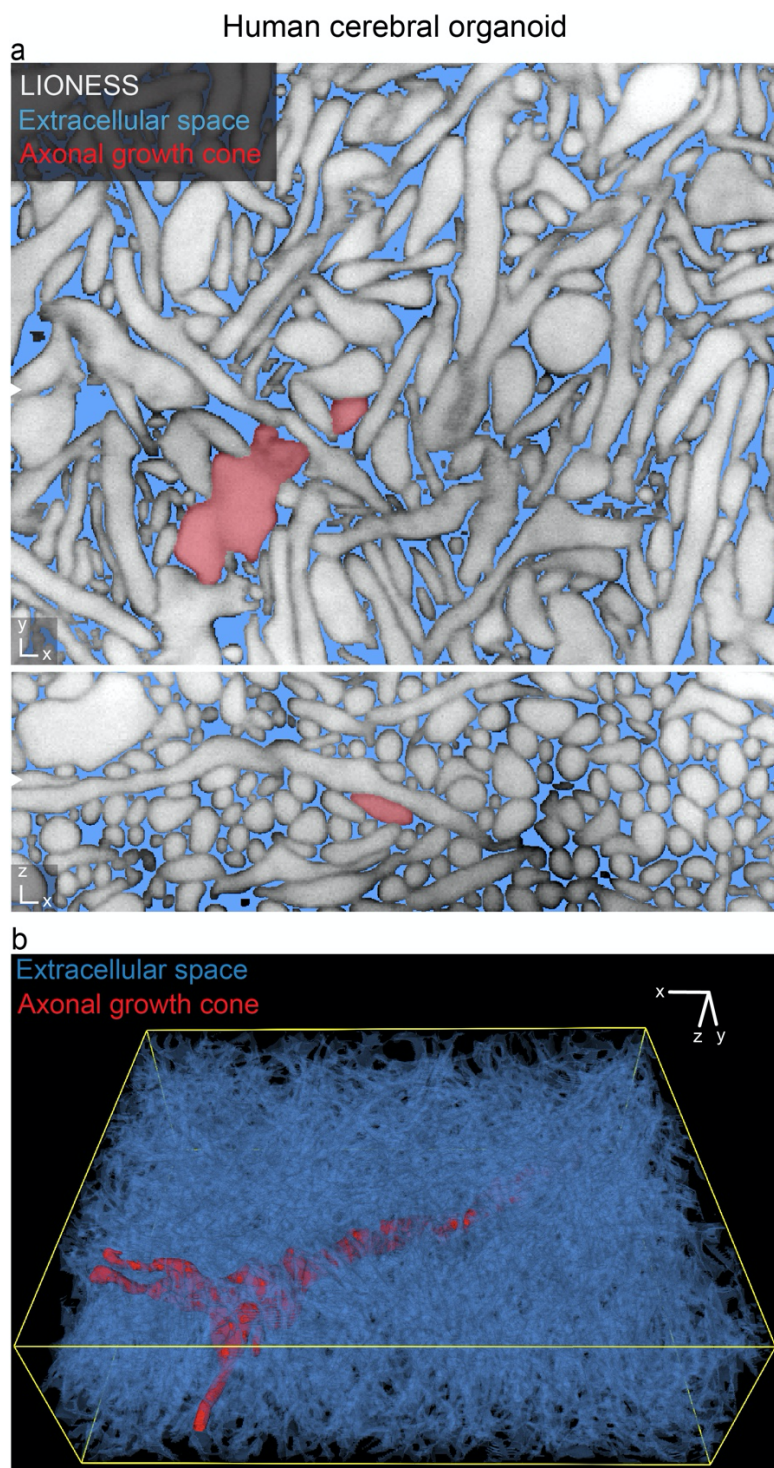
Supplementary Fig. 7

Manual segmentation. LIONESS tissue volume (left), which served as basis for manual segmentation using VAST Lite 1.3.0 and 1.4.0 (right). The region in the foreground shows a partial segmentation.



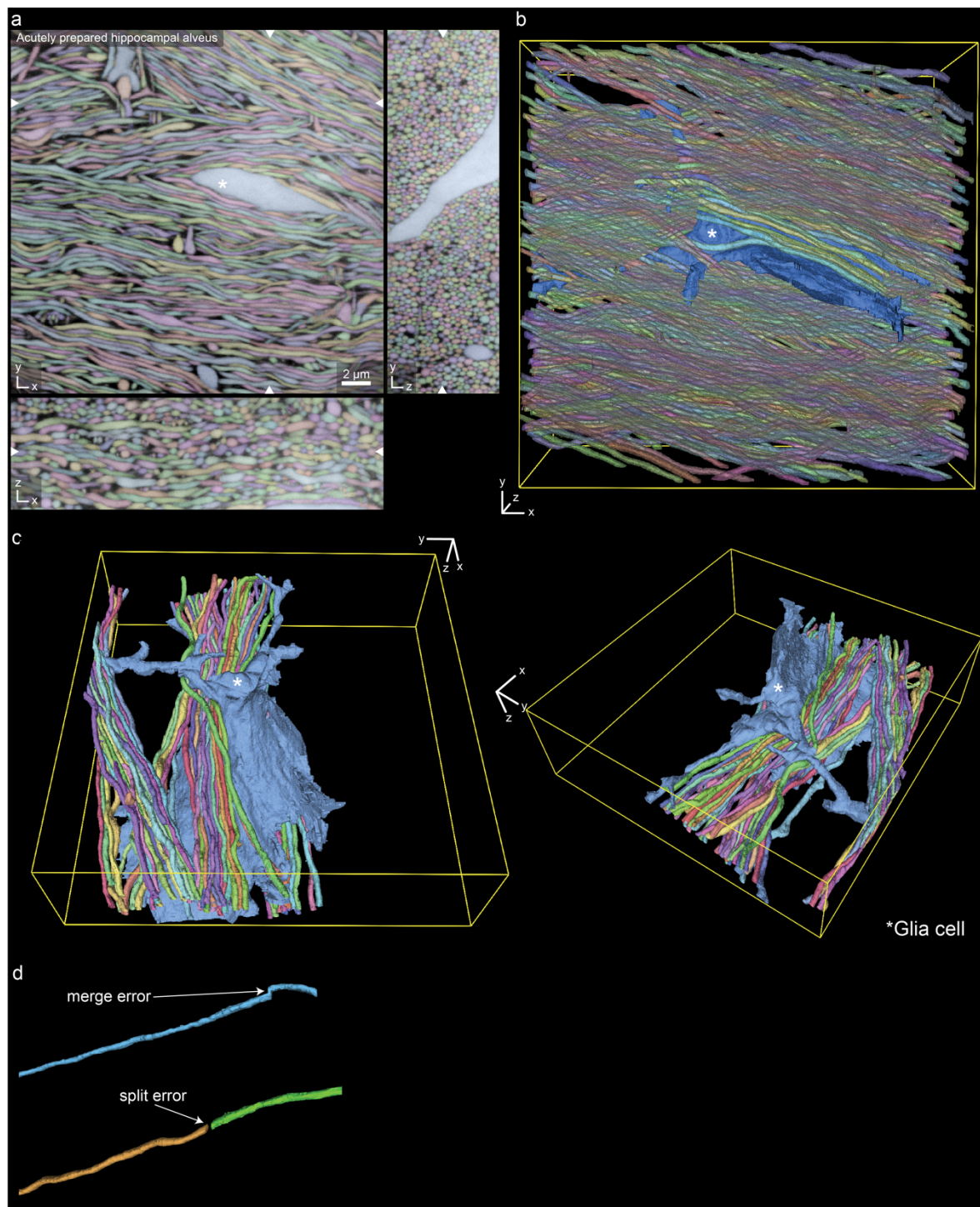
Supplementary Fig. 8

Reconstruction of living human brain organoid. a, LIONESS volume of the human cerebral organoid in Fig. 1, eroded to reveal an axonal growth cone transmigrating the dense tissue and a selection of the structures it interacts with (left). Right: The same growth cone depicted from another angle. **b**, Top view of the saturated organoid reconstruction in Fig. 1. **c**, Exploded view of the same saturated reconstruction.



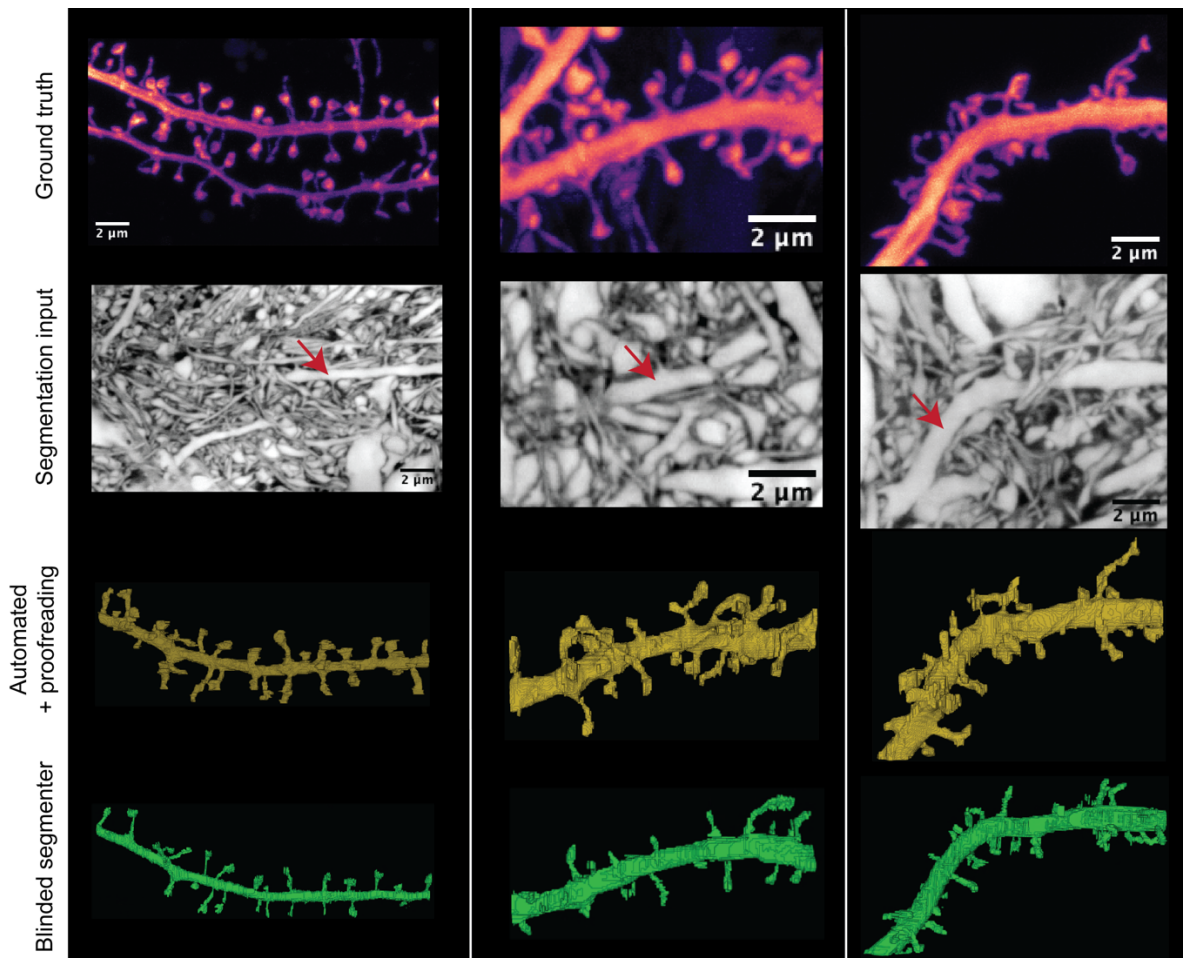
Supplementary Fig. 9

3D-segmentation of extracellular space. **a**, Orthogonal views of the LIONESS data from the human cerebral organoid in **Fig. 1**. LIONESS data is shown in gray, the same axonal growth cone as in **Suppl. Fig. 8** is highlighted in red and the extracellular space in blue. White arrowheads indicate corresponding orthogonal planes. **b**, 3D-reconstruction of the extracellular space (blue) with the axonal growth cone (red).



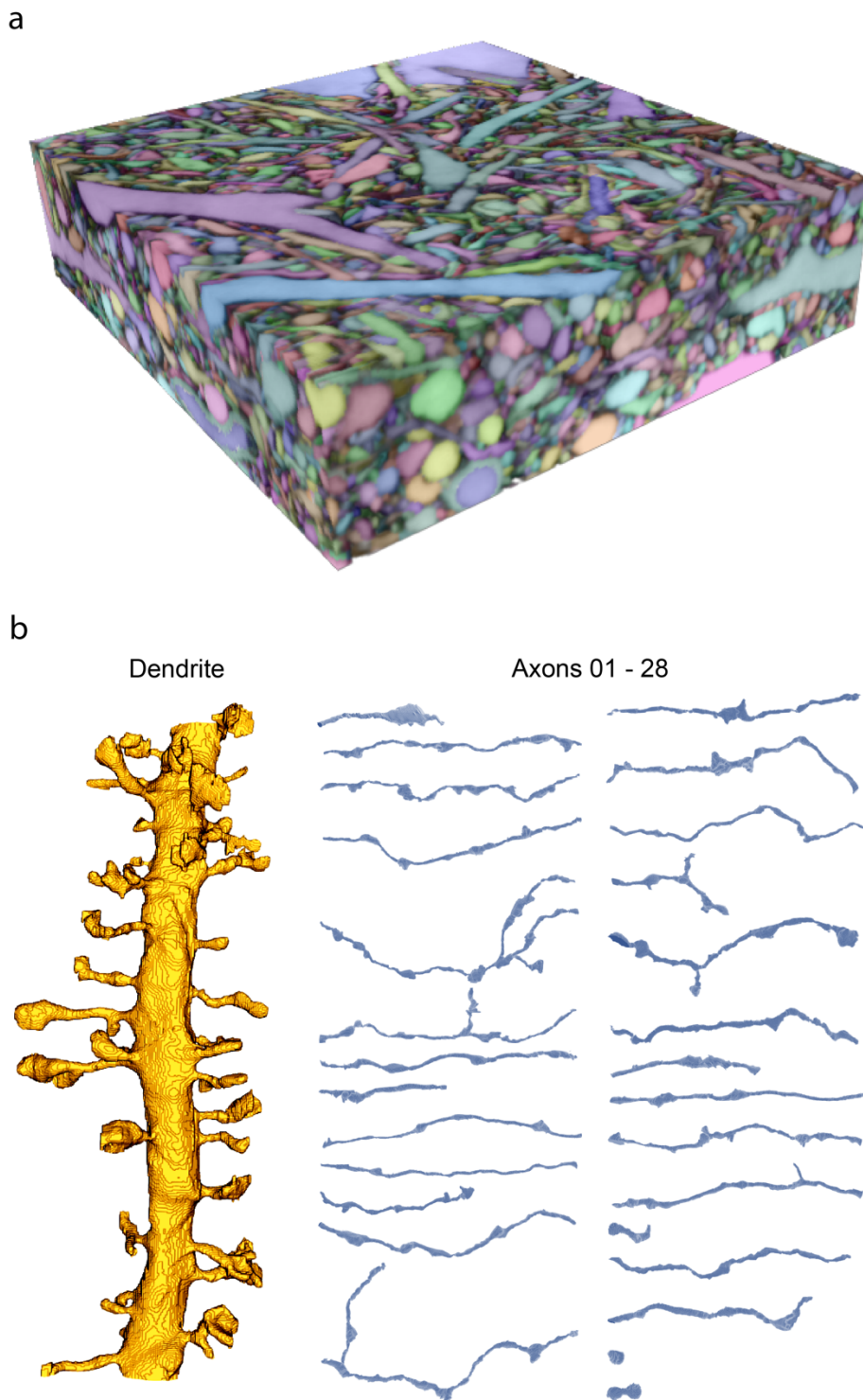
Supplementary Fig. 10

Reconstruction of living hippocampal alveus. **a**, Three orthogonal planes from a fully segmented LIONESS volume in acutely prepared mouse alveus. The white asterisk indicates a glia cell stretching through dense axons. White arrowheads at image edges indicate the position of orthogonal xy -, yz - or xz -views. **b**, 3D-rendering of a subset of structures from the same dataset as shown in panel **a**. **c**, 3D-reconstruction of the glia cell marked in panel **a** and selected axons, viewed from two different angles. **d**, Examples of error types after automated segmentation.



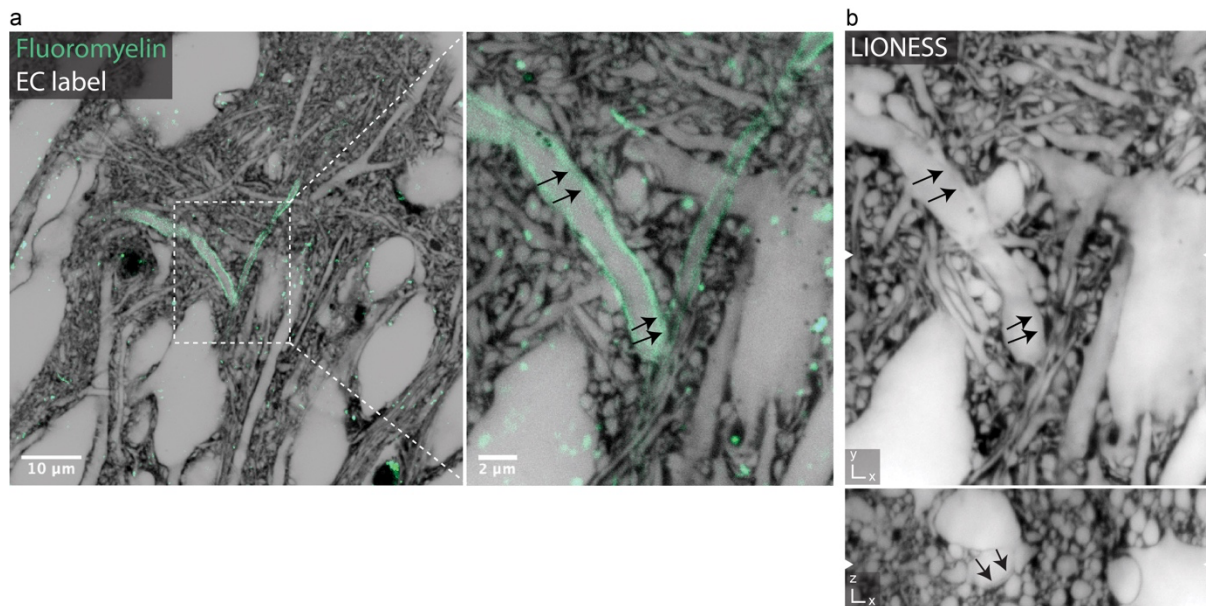
Supplementary Fig. 11

Validation of LIONESS segmentation. Top row: Maximum intensity projections of positively labeled (Thy1-EGFP) dendrites in 3 different samples from hippocampus, serving as sparse ground truth for LIONESS segmentations. Scale bars: 2 μm . Second from top: Volumetric LIONESS acquisitions used as source data for segmentation. Red arrows indicate the dendrites corresponding to the positively labelled structure above. Third from top: 3D-reconstructions of LIONESS data with automated segmentation and additional proofreading by the experimenter who recorded the data (i.e. non-blinded to the EGFP channel). Bottom: Fully manual spine detection from LIONESS data by a segmenter blinded to the EGFP-channel.



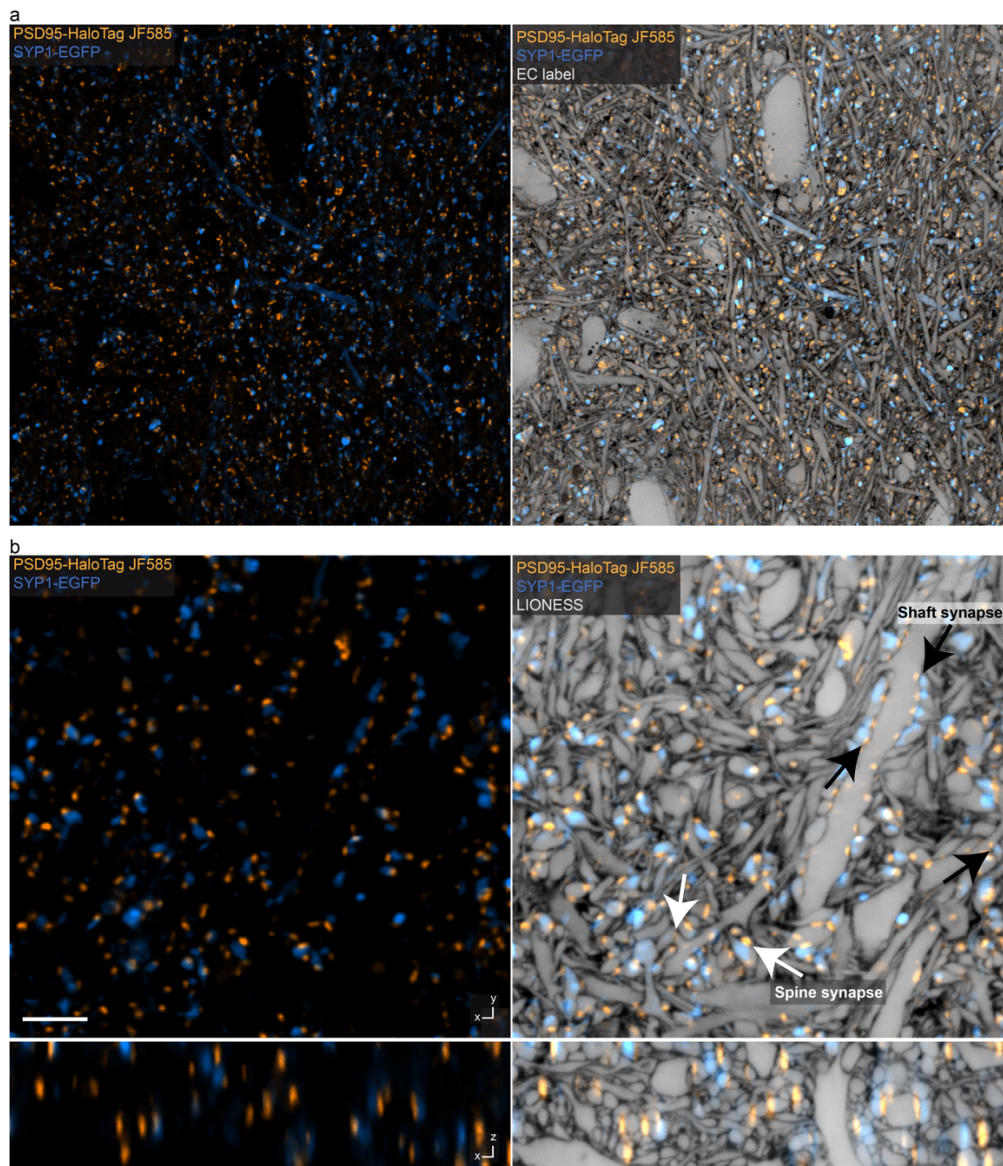
Supplementary Fig. 12

Reconstruction of spiny dendrites and connected axons. **a**, The whole, fully segmented dataset from Fig. 3, partially proofread. Volume dimensions: $23.2 \times 22 \times 6 \mu\text{m}^3$. **b**, Spiny dendrite and the 28 individual connected axons from Fig. 3 without surface smoothing. The two short segments in the bottom right correspond to one bouton right at the edge of the imaging volume and one bouton which could not be unambiguously assigned to an axon.



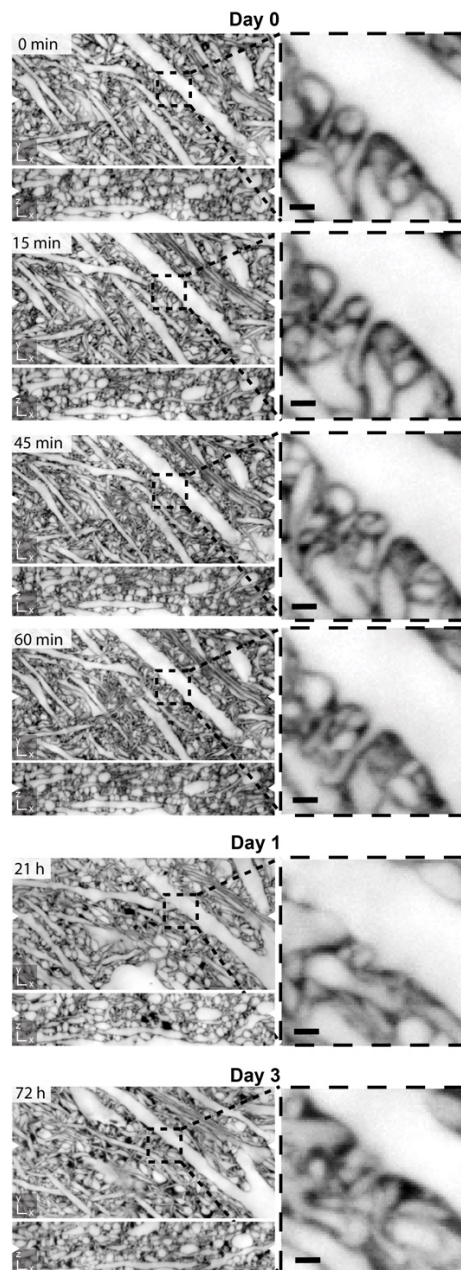
Supplementary Fig. 13

Identification of myelinated axons. **a**, ECS (gray, inverted LUT) and myelin (green) labelled confocal overview image in organotypic hippocampal slices. The magnified view (right) highlights a myelinated axon. Single plane in isotropically resolving STED mode for extracellular label and confocal mode for the myelin stain (Fluoromyelin). **b**, Volumetric LIONESS acquisition of the same region. Black arrows indicate the border between axon and myelin sheath visible in the LIONESS data. White arrowheads at image edges indicated the corresponding position of xy - or xz -views. LIONESS images are maximum intensity projections spanning 150 nm.



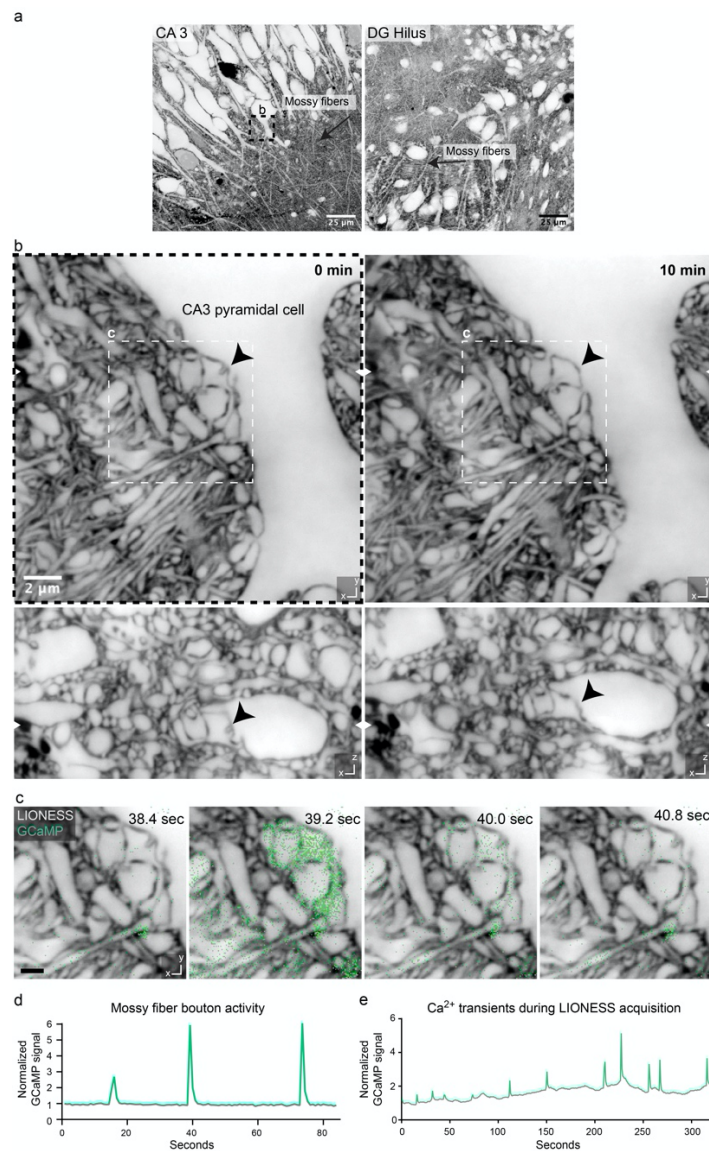
Supplementary Fig. 14

Structural and molecular information. a, Overview image of CA1 hippocampal neuropil in living organotypic brain slice from a transgenic mouse line expressing post synaptic density protein 95 (PSD95)-HaloTag to label postsynapses (orange, STED). A subset of presynapses were labelled by a synaptophysin 1 (SYP1)-EGFP fusion protein, encoded by a pseudotyped rabies virus (blue, confocal). Left: Molecular markers. HaloTag labelled with JF585. Right: Same region with structural context from additional extracellular labeling (STED). Scale bar: 10 μ m. **b**, Orthogonal planes in xy - and xz -direction of an imaging volume in CA1 from a different sample. Labeling and colour coding as in panel a. Left: Confocal imaging after denoising. Right: Additional overlay with isotropically super-resolved LIONESS data, clarifying the relationship of molecularly defined entities (pre- and postsynapses) with cell- and tissue- structure. Diffraction-limited signals extend beyond corresponding structures recorded in LIONESS mode, particularly evident in the xz -view. White arrows indicate excitatory spine synapses, black arrows indicate excitatory shaft synapses. LIONESS images correspond to maximum intensity projections spanning 150 nm.



Supplementary Fig. 15

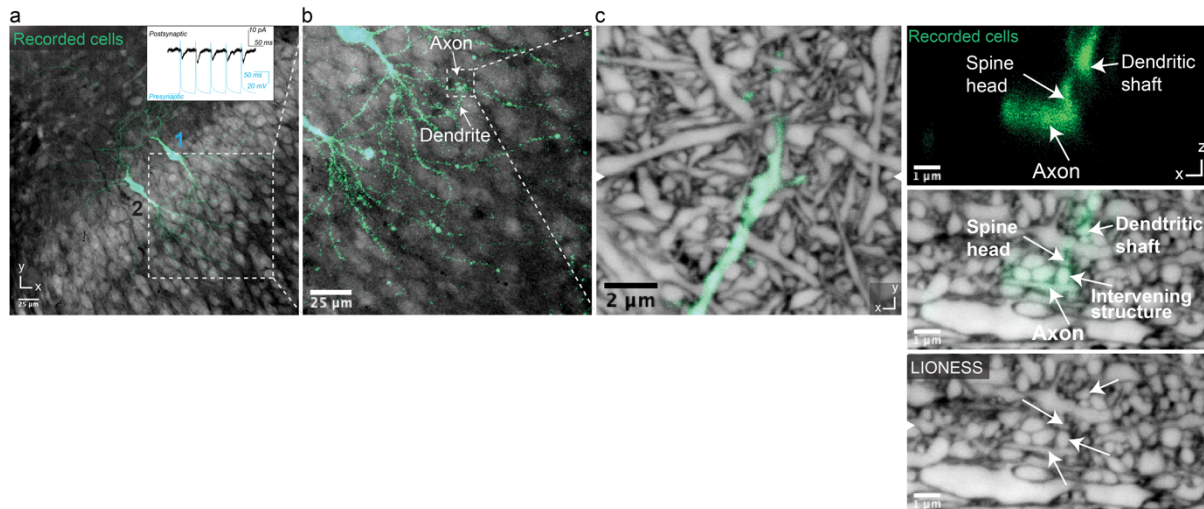
Structural dynamics in repeated volumetric LIONESS acquisition. Corresponding orthogonal planes in xy - and xz -direction from 6 consecutive measurements of the same tissue volume with LIONESS. The volume in an organotypic hippocampal slice was initially imaged 4 times within one hour and then again after one day and after three days, indicating tissue viability after repeated volumetric LIONESS imaging. Magnified views focus on a subregion with dendritic spines revealing morphodynamics. Scale bars, overview: $3\mu\text{m}$, magnified views: 500 nm . White arrowheads at image edges indicate the position of corresponding orthogonal planes. Maximum intensity projections spanning 150 nm . Additional dark regions on day 1 and day 3 likely represent branched processes of a damaged cell that took up dye after repeated manual mounting of the sample, supported by a membrane for interface tissue culture, transfer to the microscope, volumetric imaging, unmounting, and transfer back to the tissue culture incubator.



Supplementary Fig. 16

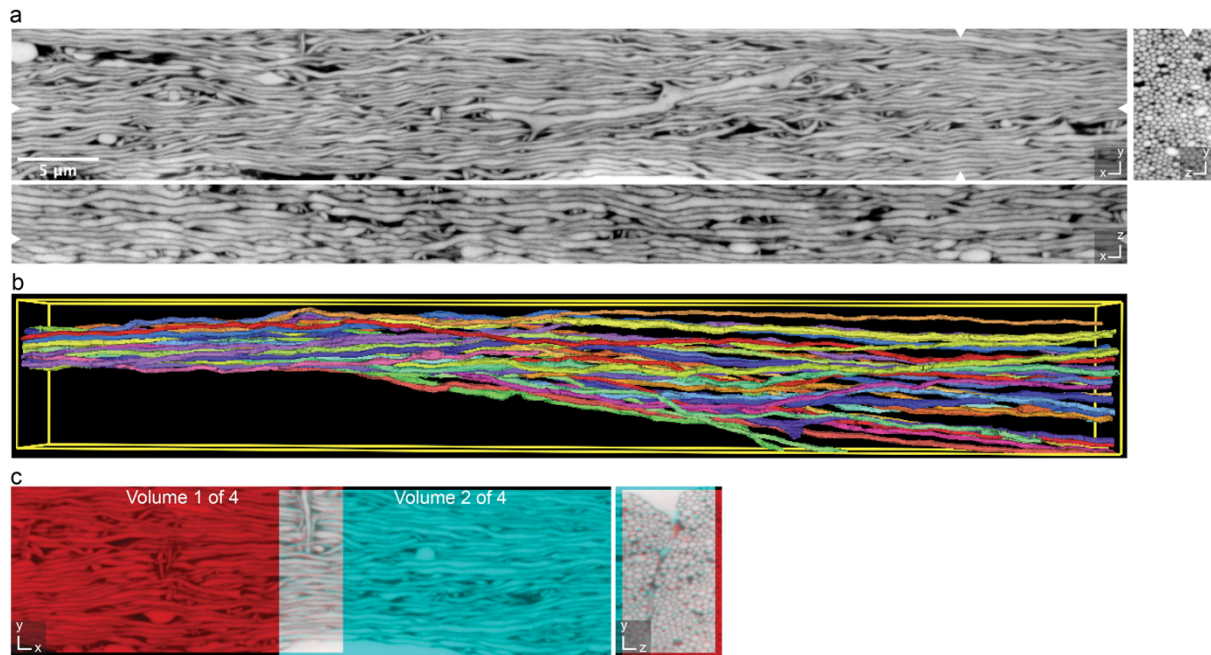
Correlating structure and morphodynamics with Ca²⁺-activity.

a, Overview images in hippocampus with mossy fibres conveying excitatory input from DG granule cells (right) to CA3 pyramidal neurons (left). Scale bar: 25 μ m. **b**, Volumetric LIONESS acquisitions at two timepoints (left: 0 minutes, right: 10 minutes) revealed morphodynamics of the complex interface between pre- and post-synaptic structures. The black arrowhead marks a structure changing over time. White arrowheads at image edges indicate the corresponding positions of *xy*- and *xz*- views. Scale bar: 2 μ m. **c**, Plane from the LIONESS volume overlaid with diffraction-limited signal from the calcium indicator GCaMP6s (green). LIONESS images are identical replicates providing structural context to the time-varying Ca²⁺-signals. Scale bar: 1 μ m. **d**, Normalized GCaMP signal of the mossy fibre bouton shown on panel c as a function of time. **e**, GCaMP signal as a function of time (and location) recorded as an additional colour channel with the volumetric LIONESS acquisition for timepoint 0 min in panel b, indicating that Ca²⁺-activity continued during LIONESS acquisition. LIONESS images are maximum intensity projections spanning 150 nm.



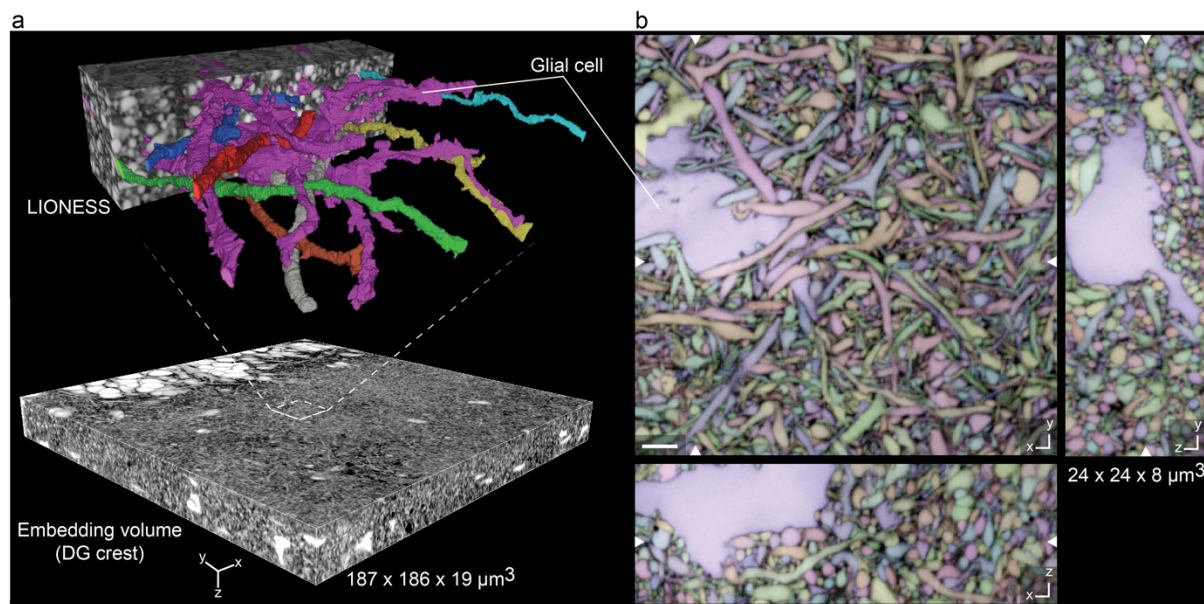
Supplementary Fig. 17

Correlating structural with electrophysiological information. **a**, Two CA1 pyramidal neurons after patch clamp recording and filling with fluorescent dye in organotypic hippocampal slice culture. Currents in neuron (2) elicited by triggered action potentials in neuron (1) reveal a synaptic connection in the paired recording (inset). Scale bar: 25 μm . Confocal images of positively labelled neurons (green) and extracellular label (grey) with low-numerical aperture objective. **b**, Region where axon of neuron 1 overlaps with a dendrite of neuron 2, suggesting a synaptic connection in confocal imaging. Scale bar: 25 μm . **c**, Detailed view of overlap region with positively labelled structures (green) read out at diffraction-limited resolution with a high-numerical aperture objective, embedded in surrounding volume recorded with LIONESS. Orthogonal views in xy - and xz -directions, with arrowheads indicating the corresponding orthogonal section. The diffraction-limited xz -view of the positively labelled structures indicated a synaptic connection (top). The increased resolution and comprehensive labelling of all cellular structures in the LIONESS xz -view disclosed an intervening structure unrelated to the two patch-clamped neurons. Scale bars, xy -view: 2 μm , xz -view: 1 μm . Maximum intensity projections spanning 150 nm.



Supplementary Fig. 18

Extending LIONESS tissue volumes. **a**, Orthogonal planes in xy -, xz -, and yz -directions from a LIONESS volume in acutely prepared mouse alveus. Data were registered from 4 consecutive, partially overlapping acquisitions. White arrowheads indicate position of corresponding orthogonal planes. Maximum intensity projections spanning 150 nm. **b**, 3D-rendering of selected axons from panel a, forming a tight bundle in the left and progressively fanning out. **c**, Example of alignment between two of the partially overlapping subvolumes in xy - and yz -views. Individual subvolumes are shown in red and cyan, such that overlapping regions add up to white colour, indicating the degree of overlap.



Supplementary Fig. 19

Meso-scale tissue context. **a**, Meso-scale overview volume acquired in diffraction-limited mode with select subvolume acquired and reconstructed using LIONESS in an organotypic hippocampal slice. A glial cell and its spatial interplay with exemplary neuronal processes is 3D-rendered. **b**, Three orthogonal planes from the automated segmentation of the LIONESS volume in panel a. Segmentation (colour) and LIONESS data are overlaid. No proofreading was applied. White arrowheads indicate corresponding orthogonal planes. The same glial cell is indicated in both panels. Scale bar: 2 µm.

Supplementary Video 1

LIONESS volume in living hippocampal alveus - 1 (xy view).

Full stack (xy-planes) of the acutely prepared mouse alveus LIONESS dataset shown in Suppl. Fig.

10. Step size is 50 nm (160 optical sections).

Supplementary Video 2

LIONESS volume in living hippocampal alveus - 2 (yz view).

Full stack (yz-planes) of the acutely prepared mouse alveus LIONESS dataset shown in Suppl. Fig.

10. Step size is 50 nm (500 optical sections).

Supplementary Video 3

LIONESS volume in living hippocampal neuropil - 1 (xy view).

Full stack (xy-planes) of the organotypic slice culture neuropil LIONESS dataset shown in Fig. 3.

Step size is 50 nm (120 optical sections).

Supplementary Video 4

LIONESS volume in living hippocampal neuropil - 2 (xz view).

Full stack (xz-planes) of the organotypic slice culture neuropil LIONESS dataset shown in Fig. 3. Step

size is 50 nm (440 optical sections).

Supplementary Video 5

Molecularly informed LIONESS volume in living hippocampal neuropil

Full stack (xy-planes) of the whole PSD95 and synaptophysin labelled LIONESS dataset shown cropped in Fig. 4. Step size is 50 nm (120 optical sections).

Supplementary Video 6

GCaMP recording, overview

Diffraction limited recording of calcium transients using EC labelled (Atto 643) Ai95/Prox1-cre mouse organotypic hippocampal slice cultures. Depicted is one plane of a region of the DG during gabazine application. Acquisition frame rate was 1.25 Hz.

Supplementary Video 7

GCaMP recording, single synapse

Full series of the GCaMP recording after gabazine application shown in Suppl. Fig. 16c. LIONESS images are identical replicates providing structural context to the time-varying Ca^{2+} -signals (green). Acquisition frame rate of the GCaMP signal was 1.25 Hz.

Supplementary Video 8

GCaMP recording, chemogenetically activated single synapse

Full series of the GCaMP recording shown in Fig. 5 a. LIONESS and DREADD (hM3Dq, orange) images are identical replicates placing the overlaid time-varying Ca^{2+} -signals (green) after stimulation with the DREADD ligand CNO into structural context. Acquisition frame rate of the GCaMP signal was 2 Hz.

Supplementary Video 9

LIONESS volume in living hippocampal dentate gyrus - 1 (xy view).

Full stack (*xy*-planes) of the organotypic slice culture LIONESS dataset in the dentate gyrus shown in Suppl. Fig. 19. Step size is 50 nm (160 optical sections).

Supplementary Video 10

LIONESS volume of hippocampal DG crest - 2 (xz view).

Full stack (*xy*-planes) of the organotypic slice culture LIONESS dataset in the dentate gyrus shown in Suppl. Fig. 19. Step size is 50 nm (480 optical sections).